Citation for published version:
Johnson, A, Guc, M, Andrade-Arvizu, J, Ahmet, IY, Oliva, F, Placidi, M, Saucedo, E, Pérez-Rodríguez, A & Izquierdo-Roca, V 2020, 'Structural and vibrational properties of - and -SnS polymorphs for photovoltaic applications', *Acta Materialia*, vol. 183, pp. 1-10. https://doi.org/10.1016/j.actamat.2019.11.016

DOI:
10.1016/j.actamat.2019.11.016

Publication date:
2020

Document Version
Peer reviewed version

Link to publication

Publisher Rights
CC BY-NC-ND

University of Bath

Alternative formats
If you require this document in an alternative format, please contact:
openaccess@bath.ac.uk

General rights
Copyright and moral rights for the publications made accessible in the public portal are retained by the authors and/or other copyright owners and it is a condition of accessing publications that users recognise and abide by the legal requirements associated with these rights.

Take down policy
If you believe that this document breaches copyright please contact us providing details, and we will remove access to the work immediately and investigate your claim.

Download date: 17. Nov. 2020

Elsevier Editorial System(tm) for Acta Materialia

Manuscript Draft

Manuscript Number: A-19-1914R2

Title: Structural and vibrational properties of α- and π-SnS polymorphs for photovoltaic applications

Article Type: Full length article

Keywords: SnS, thin films, X-ray diffraction, Raman spectroscopy

Corresponding Author: Dr. Maxim Guc, Ph.D.

Corresponding Author's Institution: Catanonia Institute for Energy Seresearch - IREC

First Author: Maxim Guc, Ph.D.

Order of Authors: Maxim Guc, Ph.D.; Jacob Andrade-Arvizu; Ibrahim Ahmet; Florian Oliva; Marcel Placidi; Xavier Alcobe; Edgardo Saucedo; Alejandro Pérez-Rodríguez; Andrew Johnson; Victor Izquierdo-Roca

Abstract: Tin sulphide (SnS) has attracted the attention of the photovoltaic (PV) community due to the combination of desirable optical properties, and its binary and earth abundant elemental composition, which should lead to relatively simple synthesis. However, currently the best SnS based PV device efficiency remains at 4.36 %. Limited performance of this material is attributed to band gap alignment issues, deviations in doping concentration and poor film morphology. In this context Raman spectroscopy (RS) analysis can be useful as it facilitates the accurate evaluation of material properties. In this study we present a RS study, supported by X-ray diffraction and wavelength dispersive X-ray measurements, of α- and π-SnS thin films. In particular a complete description of SnS vibrational properties is made using six excitation wavelengths, including excitation energies coupled with certain optical band to band transitions, which leads to close to resonance measurement conditions. This study describes an in-depth analysis of the Raman spectra of both SnS structural polymorphs, including the differences in the number of observed peaks, with their relative intensities and Raman shift. Additionally, we evaluate the impact of low temperature heat treatment on SnS. These results explicitly present how the variation of the [S]/[Sn] ratio in samples deposited by different methods can lead to significant and correlated shifts in the relative positions of Raman peaks, which is only observed in the α-SnS phase. Furthermore, we discuss the suitability of using Raman spectroscopy based methodologies to extract fine stoichiometric variations in different α-SnS samples.

COVER LETTER

Dear Editor and Referees,

The attached files include our revised manuscript entitled “Structural and vibrational properties of α- and π-SnS polymorphs for photovoltaic applications”, by M. Guc et al., that is submitted for publication in Acta Materialia journal.

Please address to me on the email below for any further information.

Sincerely,

Maxim Guc, PhD
Catalonia Institute for Energy Research (IREC)
e-mail: mguc@irec.cat

ANSWERS TO THE REVIEWERS' COMMENTS

We would like to thank Referee for the clarification of his comment. The answers to the Referee's comment is followed. Changes in the new revised version are highlighted with green together with changes from the first revision highlighted with yellow.

Reviewer #1:

The authors have addressed all comments, and their responses to comments 2-5 are very well accepted. However, the response to comment 1 is lacking. This may be due to misunderstanding my comment, which I would like to clarify: the [S/Sn] ratio in figure 8 is indeed determined by eq. 4, as also noted in the original comment, which indeed refers to the shift of the Raman peak of the relevant phase (only). However, eq. 4 was deduced from figure 7, in which this ratio was determined as noted in the original comment: This ratio is calculated from the measured [S]/[Sn] ratio in the films (by WDS), by accounting for the effect of other phases, detected in the film by XRD, on the measured [S]/[Sn] ratio. The hidden assumption, as I understand it, is that only the SnS phase deviates from the stoichiometric [S]/[Sn] ratio, while the composition of the other phases is strictly stoichiometric.

The following revision was therefore not addressed: The authors should provide evidence for that assumption, otherwise this correlation is incorrect (and/ or better explain the calculation of the [S]/[Sn] ratio in the SnS phase from the measured [S]/[Sn] ratio of the films). As this analysis is central to the conclusions drawn in the paper, I believe this issue should be addressed before the manuscript is accepted.

Answer: *The Referee is correct that presence of the secondary phases and their possible off-stoichiometry in the set of thin films deposited by CVT method are extremely critical for the correct determination of the coefficients in Eq. (4). However the used WDX method for the composition estimation is a punctual method of analysis of the composition with spot size lower than 100 nm. In this case the measurements were performed to avoid the grains with a highly distinct brightness, which can be explained by the formation of secondary phases. The distribution of the secondary phase crystallites can be seen in the SEM image below, and as we mentioned, these were not taking into account during the compositional analysis of the SnS phase. The statement about this was added to the end of Experimental details, page 7:*

*"*Note that the regions in with a distinctively brighter contrast were assigned to the generation of secondary phases (i.e. Sn_2S_3 and SnS_2) on the SnS surface and these grains were avoided during WDX elemental analysis in order to directly probe the stoichiometry of the SnS films.*"*

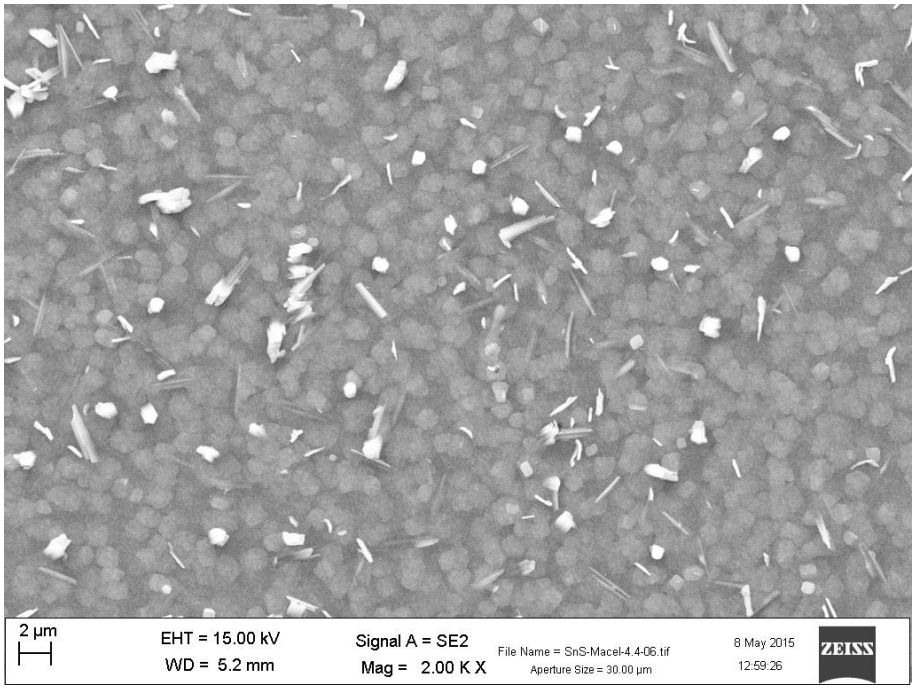

*Additionally, in the original manuscript we have written: "...*to obtain strict equations describing the dependencies a set of reference samples should be analysed, where composition was measured with a high precision.*", and as it follows from both Abstract and Conclusions of the work we are not pretending to present the strict correlation of the Raman peaks position with the [S]/[Sn] ratio, but only underline the possibility to develop a useful methodology based on Raman spectroscopy.*

*Manuscript
Click here to download Manuscript: Manuscript_rev2_v1.docx Click here to view linked References

Structural and vibrational properties of α- and π-SnS polymorphs for photovoltaic applications

Maxim Guc[1*], Jacob Andrade-Arvizu[1], Ibbi Y. Ahmet[2], Florian Oliva[1], Marcel Placidi[1], Xavier Alcobé[3], Edgardo Saucedo[1], Alejandro Pérez-Rodríguez[1,4], Andrew L. Johnson[2], Victor Izquierdo-Roca[1]

[1]Catalonia Institute for Energy Research (IREC), Sant Adrià del Besòs-Barcelona, Jardins de les Dones de Negre 1 2pl., 08930, Spain.

[2]Department of Chemistry and Centre for Sustainable Chemical Technologies, University of Bath, Claverton Down, Bath, BA2 7AY, United Kingdom.

[3]Centres Cientifics i Tecnologics CCiTUB, Universitat de Barcelona, C. Lluis Sole i Sabarís 1, 08028, Barcelona, Spain.

[4]IN[2]UB, Departament d'Electrònica, Universitat de Barcelona, Martí i Franquès 1, 08028 Barcelona, Spain.

*Corresponding author. E-mail: mguc@irec.cat

Abstract

Tin sulphide (SnS) has attracted the attention of the photovoltaic (PV) community due to the combination of desirable optical properties, and its binary and earth abundant elemental composition, which should lead to relatively simple synthesis. However, currently the best SnS based PV device efficiency remains at 4.36 %. Limited performance of this material is attributed to band gap alignment issues, deviations in doping concentration and poor film morphology. In this context Raman spectroscopy (RS) analysis can be useful as it facilitates the accurate evaluation of material properties. In this study we present a RS study, supported by X-ray diffraction and wavelength dispersive X-ray measurements, of α- and π-SnS thin films. In particular a complete description of SnS vibrational properties is made using six excitation wavelengths, including excitation energies coupled with certain optical band to band transitions, which leads to close to resonance measurement conditions. This study describes an in-depth analysis of the Raman spectra of both SnS structural polymorphs, including the differences in the number of observed peaks, with their relative intensities and Raman shift. Additionally, we evaluate the impact of low temperature

heat treatment on SnS. These results explicitly present how the variation of the [S]/[Sn] ratio in samples deposited by different methods can lead to significant and correlated shifts in the relative positions of Raman peaks, which is only observed in the α-SnS phase. Furthermore, we discuss the suitability of using Raman spectroscopy based methodologies to extract fine stoichiometric variations in different α-SnS samples.

Keywords: SnS, thin films, X-ray diffraction, Raman spectroscopy

1. Introduction

The high efficiency, low-cost production of solar cells by means of environmentally friendly processes is the current challenge for photovoltaic (PV) terrestrial applications. Thin film photovoltaic technologies, also known as second generation solar cells, emerged in order to meet some of these expectations by combining high conversion efficiencies with low manufacturing costs. Over the years, technologies based on different absorbers for thin film solar cells have been developed, beginning with binary materials, such as Gallium Arsenide (GaAs), Cadmium Telluride (CdTe) and then continuing with more complex solid solutions of ternary materials, such as Copper-Indium-Gallium-Selenide (CIGS) [1]. However only CIGS and CdTe based thin film solar cells have reached production level as result of costs/efficiencies competitive with established silicon based solar cell technologies. In order to meet the rising concerns about the use of expensive, rare (In and Ga), but also toxic (Cd) elements, alternative solutions quickly arose in the thin film PV research area. Earth abundant and toxic-free materials such as Copper-Zinc-Tin-Sulfo-Selenide (CZTSSe) [2] and simpler derivate such as Cu_2SnS_3 [3] and SnS [4] were investigated. Even if these compounds, at first glance, match the requirements for PV materials with suitable optical band gap, high optical absorption coefficient, high quantum yield for excited carriers; their solar conversion efficiency are still low compared to more established technologies, especially in the case of SnS-based devices (where the record efficiency is still only 4.36 % [5]).

Several studies have been conducted to understand the origins for the poor performance of SnS, and some issues have been determined. One in particular is related to the formation of single-phase samples of SnS, which can be quite challenging, since secondary stoichiometric phases (such as SnS_2, or Sn_2S_3) are also easily formed during the synthesis [4]. Another issue is that the [S]/[Sn] ratio in pure phase SnS samples is directly linked to the doping content and this has been shown to

be strongly dependant on a samples' deposition conditions [6]. Recent, studies highlight that the precise control of the [S]/[Sn] ratio in α-SnS absorber layers can lead to significant improvements in PV performance [7]. In addition, another challenge for SnS is that it can exist as different structural polymorphs (α and π), which need to be taken into account in order to optimize the performance of a SnS PV device. Even though the chemical composition and stoichiometry of the α- and π-SnS polymorphs are formally the same, the structural, physical, optical and electrical properties are sufficiently different. This is evident from the numerous publications, where the main fundamental properties of these two polymorphs are described elsewhere (follow the Refs. [8-14] for the α-SnS phase and Refs. [14-20] for the π-SnS phase).

Although, the fundamental properties of both SnS polymorphs are well known and the aforementioned limiting factors still undermine the performance of SnS in PV devices. Currently there is a lack of methodologies to screen and control the acute sensitivity of SnS to stoichiometric changes and doping content. With this in mind, Raman scattering spectroscopy can be a key to a methodology for the quality control of thin film metal chalcogenide absorber layers. Previously, Raman spectroscopy has been identified as a viable technique for the quality control of mass-produced PV materials. Thus in the case of chalcogenide-based absorber materials, the control of crystalline quality, crystal structure, chemical composition, defect concentration and phase content can be performed by analysing their Raman scattering spectra (see Ref. [21] and references therein; Refs. [22-24]). In addition, Raman-based methodologies were proposed to analyse the critical parameters of other layers in a thin film solar cells, such as thickness of a buffer layer [25,26], and charge carrier concentrations in a top contact transparent conductive oxide (TCO) layer [27,28]. However, in all cases a crucial role is played by the high quality fingerprint Raman spectra of the analysed material, and for most accurate results these may be measured under different excitation conditions, which greatly widens the possibilities and sensitivity of the proposed Raman-based methodology. The latter, known as multiwavelength Raman analysis, has already been demonstrated with a series of different materials used not only for the PV devices [29-33].

In the case of α- and π-SnS there have been a wide variety of reports on the Raman spectroscopy. Skelton et al. [34] presents an in-depth first-principles study of the lattice dynamics of the tin sulphides where they predict the Raman spectra of both α- and π-SnS polymorphs, and highlight how Raman spectroscopy could be used to identify and characterise phase impurities in tin sulphide samples. Li et al. [35] reported on the high resolution Raman mapping of SnS and

SnS/SnS_2 heterostructured nanocrystals grown by chemical vapour transport methods (CVT). In this report the authors identified a significant shift in the A_g (191.2 cm^{-1}) and B_{3g} (162.8 cm^{-1}) peaks of the α-SnS phase, which gradually red shifted to 186.8 and 158.3 cm^{-1} when measuring from the edge to the centre of the flakes composed of either α-SnS or α-SnS/SnS_2 heterostructured. They attributed this red shift to the inherent structural strain in the α-SnS nanoflakes, but are unable to pin point an exact underlying reason for such a shift [35]. Furthermore through the angular-resolved Raman intensity of the A_g mode, they also reported on the anisotropic properties of the A_g peak of SnS flakes with various thickness using 514.5 and 632.8 nm excitation wavelengths [36]. Similarly, Di Mare et al. [37] reported on the deposition of α-SnS thin films produced by thermal evaporation, and from Raman analyses the effects of substrate temperature on the as-deposited α-SnS showed no significant difference in the relative peak positions. However, post annealing of the α-SnS samples or subjecting samples to secondary deposition cycles resulted in a similar red shift in the A_g and B_{3g} relative peak positions [37].

Although some examples have been presented, we identified that only a few reports on the Raman spectrum of both SnS polymorphs [38], and none have examined these polymorphs by identifying their fingerprint Raman spectra and their resonance Raman modes. These may be identified from a wide range of excitation energies, which is the main issue of the present work. We have successfully deposited thin film samples of α- and π-SnS by aerosol assisted chemical vapour deposition (AA-CVD), and α-SnS thin films by chemical vapour transport methods (CVT), utilised for the in-depth structural and Raman scattering analysis. The second part of this study was focused on evaluating the influence of the stoichiometric [S]/[Sn] ratio in certain samples, to the Raman spectra of each SnS polymorph. From which we identified a clear correlation and shift in the A_g and B_{3g} modes with the [S]/[Sn] ratio of the α-SnS polymorph. Subsequently we propose a methodology, based on the Raman scattering spectroscopy, for the fast and non-destructive compositional evaluation of α-SnS thin films.

2. Experimental details

The first part of this study deals with the identification and assessment of SnS polymorphs. To do so, the thin films of α-SnS and the metastable π-SnS polymorph, were deposited onto FTO-coated glass substrates. The exclusive deposition of different polymorphic forms of SnS is achieved by temperature control, via an aerosol assisted chemical vapour deposition (AA-CVD) process using

a 0.08 M toluene solutions of Dimethylamido-(N-Phenyl-N',N'-Dimethyl-Thiouriate)Sn(II) dimer (TDPDT) single source precursor [14] (figure 1a). α-SnS and π-SnS were deposited at a furnace temperature of 300 and 375 °C, respectively, for 100 min.

After initial Raman analysis of the AA-CVD α-SnS and π-SnS samples, measured under different excitation wavelength, the samples were then annealed under an atmosphere of air on a hot plate for 10 min, at 6 different temperatures from 205 up to 388 °C. The samples treated with the different annealing temperatures were then analysed by XRD and Raman spectroscopy.

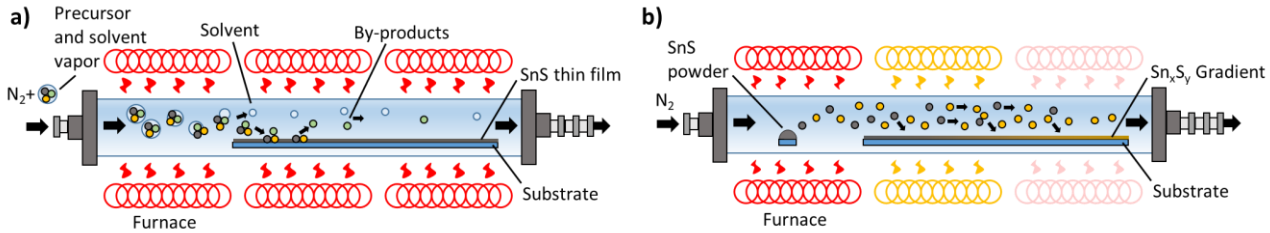

Figure 1. *Scheme presenting the two synthetises methods for the deposition of SnS thin film samples. (a) presents the selective deposition of homogeneous α- and π- SnS thin films using aerosol assisted chemical vapour deposition (AA-CVD) and (b) presents the chemical vapour transport (CVT) method resulting in a lateral gradient in the composition of α-SnS samples.*

Finally, to study in more detail the influence of the stoichiometric [S]/[Sn] ratio in α-SnS samples, a separate set of samples were deposited by chemical vapour transport methods (CVT) onto glass substrates. The [S]/[Sn] ratio was varied by synthesizing reference samples using a gradient thermal CVT system (figure 1b). For the CVT process a ceramic crucible consist of 150 mg of commercial SnS powders (Alfa Aesar 99.5 %) was positioned 20 cm from the glass substrates (soda-lime glass, SLG), in a horizontal quartz tube purged with Argon and placed in a multi zone split tube furnace. The SnS powders were heated to 580 °C and the glass substrate temperature was varied between 380 and 430 °C depending on the distance from the precursor powder (see figure 1b). The SnS vapours were carried to substrates with an Argon flow for 30 min. This resulted in the formation of a thin film gradient consisting of α-SnS with a [S]/[Sn] ratio ranging between 1.00 and 1.56.

XRD measurements were performed by means of a PANalytical X'Pert PRO MPD alpha1 diffractometer in a Bragg-Brentano θ/2θ configuration using Cu $K\alpha_1$ radiation (λ = 1.5406 Å),

selected by means of a Johansson type Ge (111) focusing primary monochromator, and an X'Celerator silicon strip 1D detector (active length of 2.113º). 2θ scans were obtained from 4 to 145º with a step size of 0.0166 º and ~1.6 seconds per step (a total measurement time of ~3.8 hours). An automatic divergence slit system and a mask enabled a constant irradiated surface (10 × 12 mm^2) over the analysed sample. The diffracting volume was constant over all the measured angular range taking into account the finite thickness of the analysed thin films. During the measurement samples were rotated at 30 rpm.

Full profile analysis, Rietveld method [39], were performed to precisely determine the cell parameters of the observed α-SnS and π-SnS, phases and in order to characterize their microstructure, obtaining the average apparent crystalline size and eventually the average microstrain, and to semi-quantify [40] the observed tin sulphide phases when mixtures were observed. The refinements were performed by the TOPAS v5 software [41,42]. The background was modelled with a 6^{th} order Chebyschev polynomial. The instrumental contribution to the diffraction profile was calculated with the Fundamental Parameters Approach [43]. The soda-glass contribution was considered by refining the area of their "observed wide peaks" as fitted in an XRD diffractogram of a soda glass reference sample. When present, the FTO phase of the underlying substrate was considered by adjusting the corresponding SnO_2 *Cassiterite* phase to the fixed structural model obtained from Seki et al. [44]. The structures of the observed tin sulphide phases were also fixed for α-SnS [11], π-SnS [17], SnS_2 [45] and Sn_2S_3 [46]. The peak width of each phase was modelled with the Double-Voigt approach by considering only the Lorentzian contribution of the crystallite size and only the Gaussian contribution to the microstrain. The Lorentzian and Gaussian averaged integral breadth are obtained from the resulting fitted Voigt function to the whole powder XRD diagram. The Scherrer and Stokes-Wilson equations [47] were then respectively applied to obtain the apparent crystallite size and microstrain. Furthermore, when necessary a preferred orientation correction was applied, as implemented in TOPAS v5 software.

Two different SnS polymorphs were examined by the Raman scattering measurements. For the 325, 442, 532, 633 and 785 nm wavelength excitations, the measurements were performed in air in backscattering configuration with a Horiba Jobin Yvon LabRam HR800-UV system. The reduced spot size used in the microscope configuration had a diameter between 1 – 2 μm. This system also allows the use of a DuoScanTM accessory which allows measuring areas of approximately 30 × 30 μm^2. For the 514.5 nm wavelengths, the measurements were performed using a T64000 Horiba

Jobin-Yvon spectrometer, in back-scattering configuration, in two modes, i.e. macro mode with a spot size of 100 μm, and micro mode with a spot size of 1 – 2 μm. The T64000 Horiba Jobin-Yvon spectrometer is equipped with the high-resolution triple monochromator which allows to avoid using the excitation wavelength filters and to measure the Raman peaks down to 20 cm^{-1} from the laser line.

To determine the chemical composition of the SnS samples, wavelength dispersive X-ray measurements (WDX) were been performed using an electron microprobe analysis JEOL-JXA 8200 EMPA system with an energy 20 keV. In order to obtain reliable results from the WDX measurements, the system was calibrated using elemental standards. High accuracy of the composition parameters was achieved by averaging over 20 local measurement points to an integral chemical composition, with an accuracy of ± 1 at.%. Note that the regions in with a distinctively brighter contrast were assigned to the generation of secondary phases (i.e. Sn_2S_3 and SnS_2) on the SnS surface and these grains were avoided during WDX elemental analysis in order to directly probe the stoichiometry of the SnS films.

3. Results and discussions

3.1 Structural and vibrational characterization of α- and π-SnS polymorphs

Figure 2 depicts the XRD patterns of α-SnS and π-SnS thin film samples deposited onto FTO coated glass substrate by AA-CVD method. In both cases the most intense diffraction peaks for the FTO substrate were detected. Both diffractograms show pure α-SnS and π-SnS polymorphs with a high crystalline quality without any evidence of elemental Sn, or SnS_2, Sn_2S_3 secondary stoichiometric phases. Additionally, no mixtures of the α-SnS and π-SnS polymorphs were observed, and only pure phases were detected for each sample. In both cases no clear crystallographic preferred orientations were detected. The resulting plots of Rietveld refinement are also presented in the figure 2 and the refinement parameters are listed in table 1.

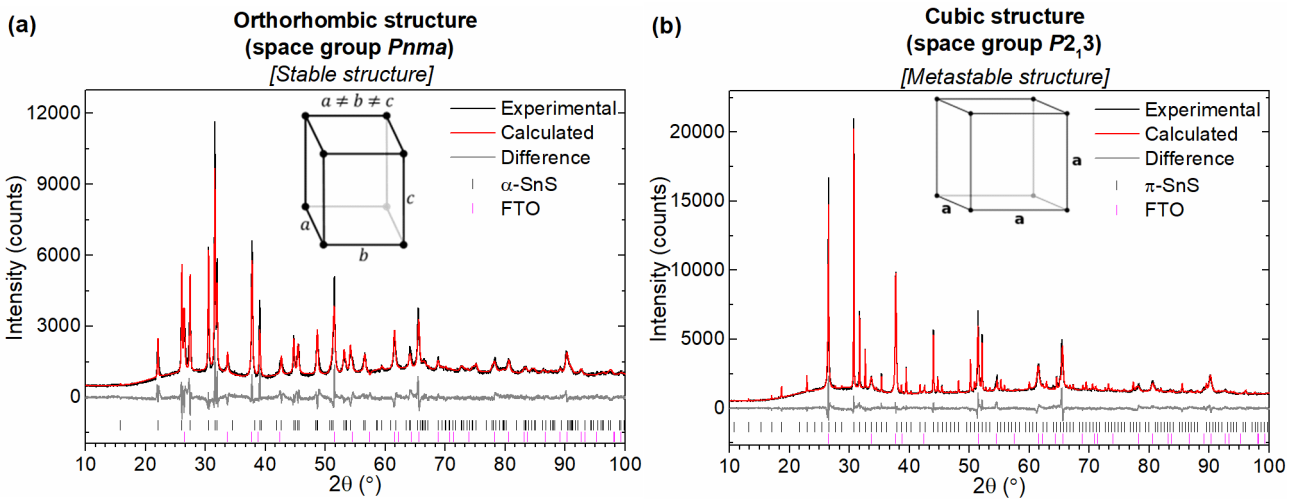

Figure 2. *Rietveld refinement of an XRD pattern of (a) α-SnS and (b) π-SnS thin films deposited onto FTO coated soda-lime glass substrates.*

Table 1. *Agreement factors, cell parameters, cell volume, volume per formula unit (V/Z) and averaged microstructure parameters obtained from the Rietveld refinements on pure α-SnS and π-SnS thin film samples.*

Phase	Structure, space group, Z	R_{wp}	R_B	*a* (Å)	*b* (Å)	*c* (Å)	V (Å^3)	V/Z (Å^3)	Apparent crystal size (nm)	Microstrain $(\delta d/d)\cdot 10^4$
α-SnS	Orthorhombic, *Pnma*, 4	6.87	3.69	11.2137	3.9917	4.3151	193.150	48.29	280	13
π-SnS	Cubic, $P3_12$, 32	5.47	2.95	11.62658	-	-	1571.65	49.11	>1000	1.2

In order to further investigate the polymorph pure α-SnS and π-SnS thin film samples, a detailed vibrational characterization by Raman spectroscopy has been performed. As previously stated, the α-SnS phase is a stable structure belonging to *Pnma* space group (mmm or D_{2h} point group), with an 8 non-equivalent atoms (Z = 4) in the primitive cell. Its irreducible representation consists of 24 vibration modes [34]:

$$\Gamma = 4A_g \oplus 2A_u \oplus 4B_{1g} \oplus 2B_{1u} \oplus 2B_{2g} \oplus 4B_{2u} \oplus 2B_{3g} \oplus 4B_{3u}, \quad (1)$$

three acoustic modes ($B_{1u} \oplus B_{2u} \oplus B_{3u}$) and twenty one optical phonon modes split into 2 inactive ($2A_u$), 7 infrared active ($B_{1u} \oplus 3B_{2u} \oplus 3B_{3u}$), and 12 Raman active ($4A_g \oplus 4B_{1g} \oplus 2B_{2g} \oplus 2B_{3g}$). Hence 12 Raman peaks are expected in the Raman spectra of α-SnS phase.

On the other hand, π-SnS phase belongs to $P2_13$ space group (23 or T point group). The primitive cell contains 64 non-equivalent atom positions (Z = 32), which results in 192 phonon modes, collecting in the following irreducible representation [34]:

$$\Gamma = 16A \oplus 16E \oplus 48T. \quad (2)$$

Here 1 triple degenerated T mode is acoustic and the other 189 modes are optical (A are non-degenerated, E are double degenerated and T are triple degenerated). All optical T modes are Raman and IR active, and the A and E modes only Raman active. This yields 126 possible peaks in Raman scattering spectra (taking into account the TO-LO splitting of T modes). The clear difference in the expected vibrational fingerprints of the α-SnS and π-SnS polymorphs is due to differences in their irreducible representations.

Figure 3 presents the Raman spectra of both α- and π-SnS polymorphs under 6 different excitation wavelengths from the UV (325 nm) to the infrared region (785 nm). As predicted by the irreducible representation, each polymorph has a specific Raman spectrum pattern which is repeated and slightly modified as the excitation wavelength increases. For the α-SnS case regardless of the excitation wavelength, four main peaks are always resolved at 96, 163, 192 and 220 cm^{-1} (in the region with wavenumber higher than 75 cm^{-1}). As the excitation energy changes the intensity ratio of these peaks is modified (e.g. see figure S1a). In total ten peaks from twelve expected from the irreducible representation analysis were observed. In Table 2, the optimal excitation wavelength and the positions of the peaks observed are summarize. The found wavenumbers are in good agreement with the experimental spectra reported by Nikolic et al. [48] and with the calculated phonon energy positions reported by Skelton et al. [34]. The comparison with the theoretical calculations allows correlating eleven modes within nine observed peaks, while one theoretical mode expected at 203 cm^{-1} is not observed and one additional peak at 286 cm^{-1} is not reported as fundamental peak for the theoretical calculations. This suggests that this peak is related to overtones, in contrast to the assignment proposed by Chandrasekhar et al. [49]. A tentative symmetry assignment proposed in the table is following the identification of the fundamental peaks reported by Skelton et al. [34]. The observed change in the peaks intensity ratio with the excitation wavelength was attributed to presence of the resonant/pre-resonant effects, as observed in other metal chalcogenide samples [29-33]. For the 325, 442 and 785 nm excitation wavelength an enhancement of the specific peaks is apparent due to the coupling of the excitation wavelength with optical active electronic transitions. It has been experimentally reported that direct band gap of α-SnS is around 1.5 eV and that there are

additional optical active transitions at 2.7 and 3.5 eV [50]. The energy value of these transitions are coupled with excitation wavelength of 785 nm (~ 1.6 eV), 442 nm (~ 2.8 eV) and 325 nm (~ 3.8 eV), respectively. On the other hand, the preferential enhancement of the peaks for the above mentioned resonant excitations are attributed to the enhancement of the specific vibrations due to the coupling of the excitation energy with the bands mainly formed by different atoms [51].

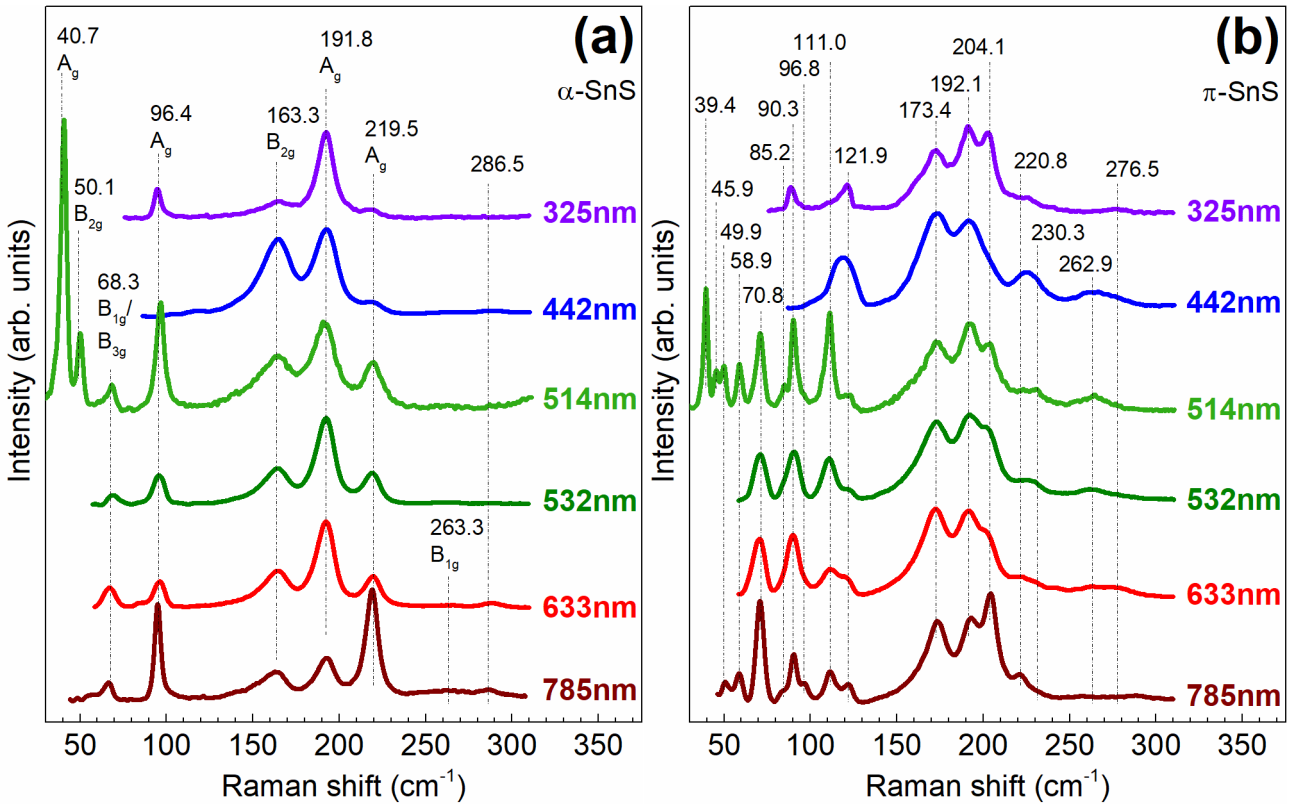

Figure 3. *Raman spectra, measured with different excitation wavelengths, for pure (a) α-SnS and (b) π-SnS thin film samples deposited by AA-CVD. The low intensity peaks in the high wavenumbers range are emphasized in the figure S1 from the Supporting Information.*

Table 2. *Position of Raman peaks of α-SnS and π-SnS phases. Results from previous experimental and theoretically calculated wavenumbers are also presented, together with proposed symmetry assignment.*

α-SnS					π-SnS				
λ* (nm)	**Exp This work (cm^{-1})**	**Exp [49,48] (cm^{-1})**	**Calc. [34] (cm^{-1})**	**Sym. [34]**	**λ* (nm)**	**Exp This work (cm^{-1})**	**Exp [38] (cm^{-1})**	**Calc. [34] (cm^{-1})**	**Sym [34]**
	40.7	40, 47	41	A_g^1		39.4		36, 36, 39	E, T, A
						45.9		43, 47, 48	T, T, E
	50.1	49, 50	48	B_{2g}^2		49.9		49, 50, 51	A, T, T
						58.9	59	54, 56, 56, 58, 59, 61, 62, 64	T, E, T, T, E, T, A, T
All	68.3	70, 58	66, 67	B_{3g}^1, B_{1g}^1	785	70.8	71	66, 68, 69, 71, 71, 72	E, A, T, T, E, T
633	77.6	85, 78	80	B_{1g}^2					
					All	85.2		79, 79, 81, 84, 86	T, A, E, A, T
					All	90.3	90	88, 89, 92	T, T, T
785	96.4	95, 111	92	A_g^2	785	96.8		98, 99, 103	T, T, T
					All	111.0	112	107, 107, 112	T, E, A
					442	121.9	123	116, 118	T, A
442	163.3	164, 160	161	B_{2g}^3					
					442	173.4	176	165, 166, 166, 168, 173, 174, 177, 178, 180, 183	A, E, T, T, A, T, E, T, T,E
532/633	191.8	192, 194	189	A_g^3	325	192.1	192	187, 195, 197	A, T, T
	–	208, –	203	B_{3g}^2	325/785	204.1	202	201, 202, 202, 207, 209, 210, 212, 214	T, T, A, T, T, E, T, E
785	219.5	218, 216	218, 220	B_{1g}^1, A_g^4	785	220.8	224	219, 220, 220, 221, 222, 224	A, E, T, A, T, T
					442	230.3		227, 229, 229, 239	T, E, T, T
785	263.3	–, 264	275	B_{1g}^2	442/432/633	262.9		242, 249, 252, 257, 257, 257, 263, 266	T, T, T, A, E, T, A, T
					325/633	276.5		269	T
633/785	286.5	290, –		A_g^2+A_g^3**					

**Optimal excitation wavelength for the assessment of the each peak. The 514.5 is discarded for its preferential polarization signal dependence due to the configuration of the system.*

***Multimode assignment proposed in this work, in contrast to the data from Ref. [49].*

As expected for the π-SnS samples, a much more complex Raman pattern was measured. In this case, 17 resolved peaks with different degree of broadening are observed. As mentioned, 126 peaks can be present in the Raman spectra of π-SnS. This high amount of expected peaks leads to strong overlapping and thus induces effective broad bands, and therefore restricts the degree of peak refinement that can be achieved (table 2).

In contrast to the Raman analysis, quite narrow Bragg reflexes were observed in XRD pattern, indicating a high crystal quality of the π-SnS sample (the crystal size ~ 1 μm). Good crystallite quality, should lead to similar narrowing of Raman peaks, which were observed for a low wavenumber peaks in the range < 125 cm^{-1}. However, as it was mentioned before, strong overlapping resulted in observed broad bands in the range > 125 cm^{-1}. The tentative symmetry assignment by comparison with calculated results in this case is also limited, as it is summarized in table 2. Furthermore, as observed in the case of α-SnS, the use of different excitation wavelengths for the π-SnS samples, brought a modification of the relative peak intensities. This is attributed to a coupling of the excitation wavelength with the different optically active transitions.

A detailed analysis of the both Raman spectra allows to observe similarities between the spectra of the two structures. In both cases two different spectral regions can be specified. First, for a low wavenumber < 150 cm^{-1} and the second, for the region between 150 and 250 cm^{-1}. The comparison with the theoretical calculations derived by Skelton et al. [34] allows identifying the first region with Sn-S vibrations and the second with pure S vibrations.

3.2 Evolution of the vibrational properties with the hot plate annealing

As previously mentioned, one of the main issues of SnS as a PV material is the lack of control over its doping, which is directly linked with its stoichiometry (i.e. [S]/[Sn] ratio) [52]. Furthermore, in depth analysis of the impact that the compositional ratio has on the vibrational and structural properties of SnS samples is not widely documented. In previous reports of SnS PV's, it has continuously been clear that there is a relationship between the [S]/[Sn] ratio in the SnS samples, with deposition temperature and the post-deposition treatment [20,53-55]. Subsequently these variables can strongly affect the performance of SnS based PV devices [20]. Considering this, using the as-deposited phase pure α-SnS and π-SnS samples deposited by AA-CVD, we performed various mild hot plate annealing treatments in air for 10 min. Figure 4 shows the corresponding XRD diffractograms and Raman spectra excited with 532 nm laser line for these various annealing

treatments. From both techniques we have observed the formation of the SnS_2 stoichiometric phase for both α- and π-polymorphs at temperatures higher than 250 °C. The formation of the SnS_2 phase can be related to the possible disproportionation of Sn^{2+}, oxidation of SnS in air, coupled with the subsequent resulfurization and high volatility of SnS at mild temperatures, where previous observations showed a significant loss of mass at ~300 ^{o}C during differential thermal analysis of π-SnS samples [54]. We therefore denote the combination of these processes to change the [S]/[Sn] ratio in these samples.

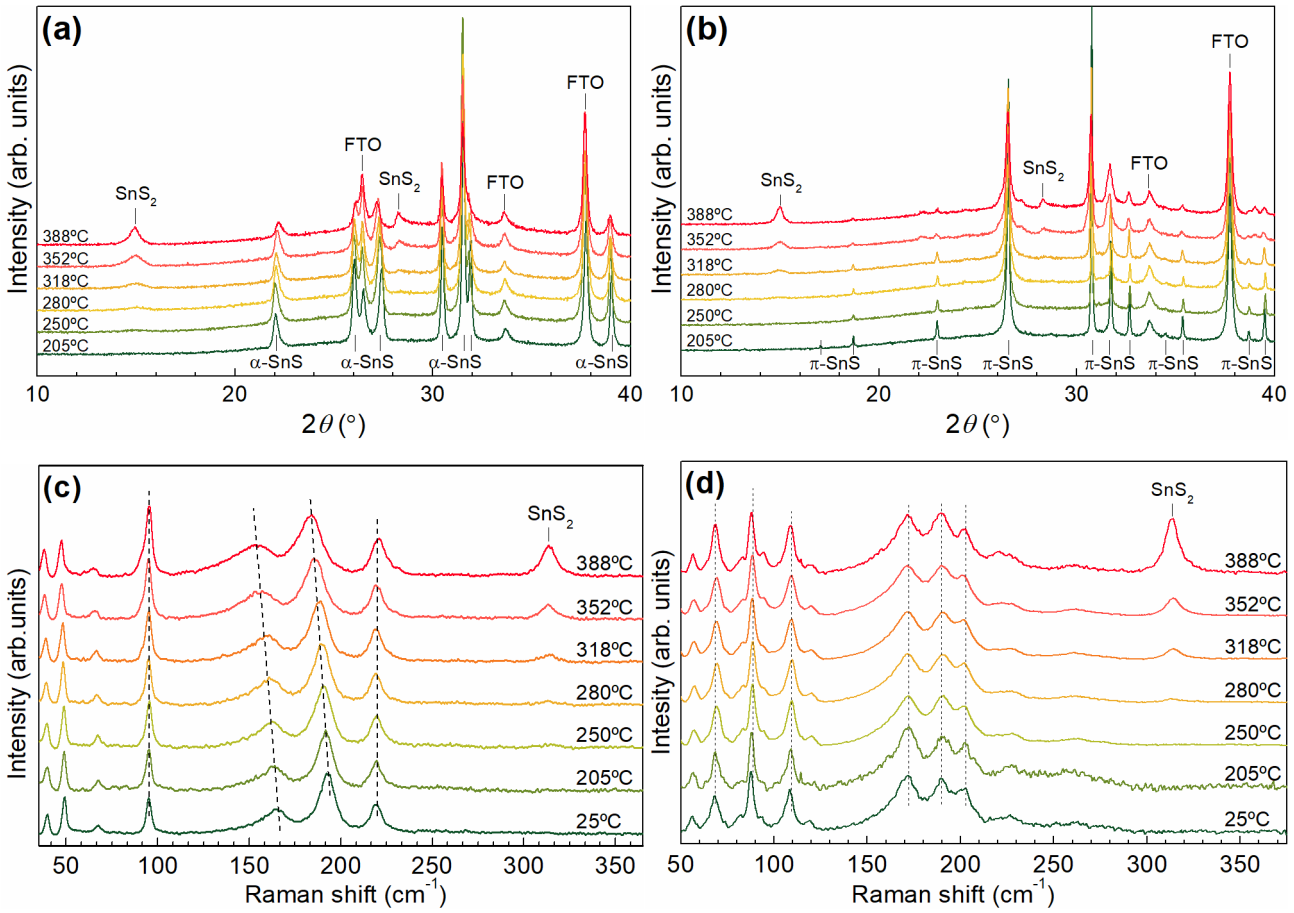

Figure 4. *Top – XRD pattern of (a) α-SnS and (b) π-SnS thin films annealed at different temperatures under air atmosphere for 10 min. Bottom – Raman spectra excited with 532 nm laser line of (c) α-SnS and (d) π-SnS thin films annealed at different temperatures under air atmosphere for 10 min.*

Interestingly, no significant shift in the peak position were observed in neither Bragg reflexes or for Raman peaks of the π-SnS samples with this mild thermal treatment in air, while a

clear dependence from annealing temperature was found for both Bragg reflexes and Raman peaks of the α-SnS polymorph. With increased annealing temperatures we present a detailed analysis for the evolution and shift of the most intense Raman peak positions for the α-SnS samples in figure 5. Peaks at 96 and 220 cm^{-1} (A_g^2 and A_g^4 respectively) showed an insignificant blue shift (blue symbols in figure 5a). The peaks with original position at 163 and 192 cm^{-1} (B^3_g and A_g modes, respectively) on the other hand presented a significant red shift in relative peak positions (red symbols in figure 5a). The blue shift of the A_g^2 and A_g^4 peaks are most probably related to the small changes crystalline quality, which can influence the width of the peaks (see the Figure S2). On the other hand, the inflexion behaviour for the B^3_g and A_g modes should have a more complex nature, related to the specific atoms sitting at the site of these vibrational modes. To further analyse this effect, Rietveld analysis of the diffractograms obtained from the α-SnS and π-SnS samples annealed at different temperatures (see the table S1) was performed and allowed us to monitor the evolution of the lattice parameters with hot plate annealing (figure 5b). Here a clear anisotropy in change of the lattice parameters of α-SnS polymorph was obtained, where *a* and *b* parameters increased and *c* parameter decreased with annealing temperature. The change of the lattice parameters leads to changes in the bond length, and as result to the change of the force constants related to the bond-stretching forces between the atoms. The phonon energy is directly proportional to the force constant, which yields the indirect proportionality with the lattice parameters. In this framework, the observed red shift of B_{2g}^2 and A_g^3 means their preferential vibration perpendicular to *c* axis, while the A_g^2 and A_g^4 modes should vibrate in *ac* (010) or *bc* (100) crystal planes, where the increase of one parameter is compensated with decrease of other.

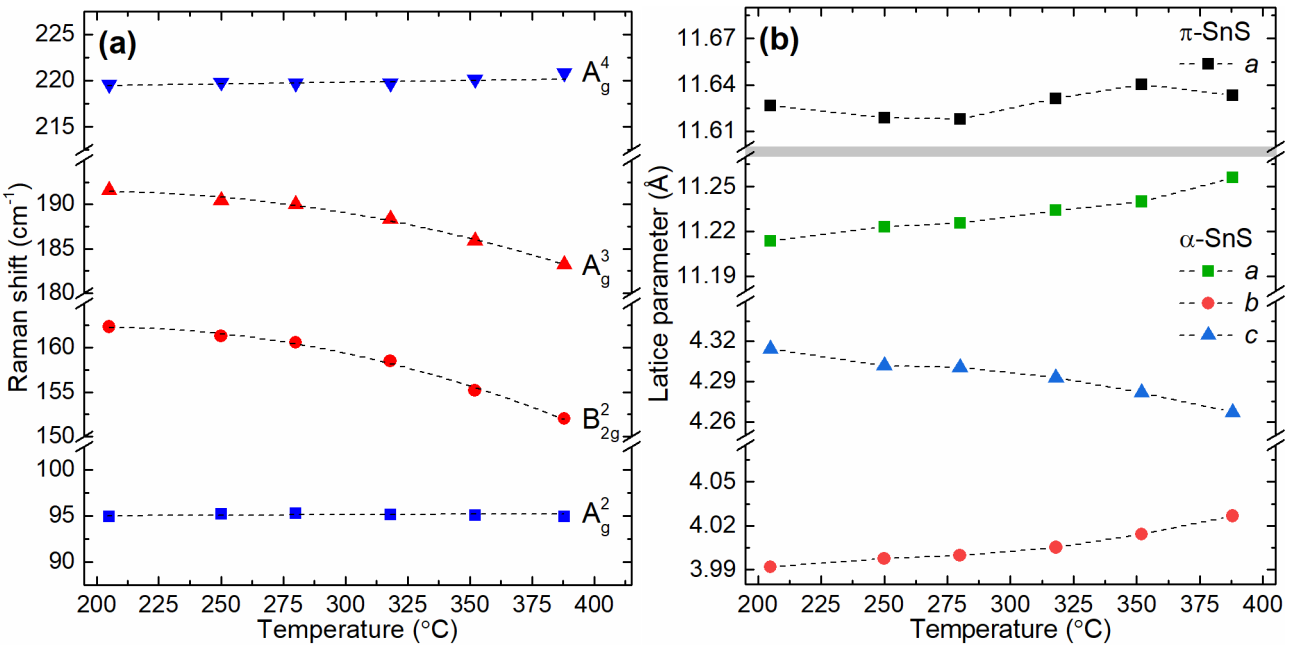

Figure 5. *(a) Shift of the main α-SnS Raman peaks positions versus different annealing temperatures. (b) Change of the lattice parameters of both SnS polymorphs versus different annealing temperatures. The errors in both graphs do not exceed the spot size.*

It should be noted, that in the case of cubic π-SnS there was not observed a trend in the change of lattice parameters with annealing temperature (see the black points in figure 5b). This leads to retention of the bond distance and force constants, and as result no change in the wavenumbers of Raman peaks is expected, and was not observed in the measured spectra (see figure S3). Additionally an amount of α-SnS phase was found in the π-SnS thin films annealed at temperatures higher than 300 °C, which is in agreement with the results of XRD analysis (see table S1), and is in accordance with higher stability of α-SnS phase. Appearance of the α-phase is hardly detected in the Raman spectra in the range 130 – 250 cm^{-1} (see figure S4), but it is undoubtedly seen from the increase of the shoulder near the peak at 90 cm^{-1}, corresponding to the peak of α-SnS phase at 96 cm^{-1} (figure S5). This supports the possibility to utilise the low wavenumber Raman peaks (in the range 80 – 125 cm^{-1}) for the assessment of mixed α- and π-polymorphs in the SnS samples, as is proposed in earlier reports [20].

3.3 Quantification of [S]/[Sn] ratio by Raman spectroscopy

The changes found in the Raman spectra of α-SnS can be used for the quantitative assessment of the [S]/[Sn] ratio, by using a calibration samples with the ratio identified by other methods. However, the previously described sets of samples are compromised by the underlying FTO-coated glass substrates. Here, the tin contained in the FTO layer increases its overall concentration measured by WDX technique and does not allow us to detect the exact values of the [S]/[Sn] ratio in the SnS thin films. In this context, we synthesized SnS thin films with different sulphur content by CVT under a linear graduated temperature profile on glass substrates (see Experimental details section). This procedure resulted in the deposition of tin sulphide films with a gradient of different [S]/[Sn] ratios. Figure 6a shows the corresponding Raman spectra of those samples. It should be noted here, that this deposition method leads to the inhomogeneous distribution of Sn and S following the direction of the Ar flow along the deposition chamber, and the substrate temperature gradually decreased at further distances from the SnS powder precursor. At lower substrate temperatures <390 ^{o}C the films remained uniform but became less homogenous in composition, as result, only in the temperature range of 430 – 390 °C (or 29 – 32 cm distance from the SnS powder precursor) the pure α-SnS phase was obtained, while as temperature decreased the formation of Sn_2S_3 and SnS_2 were observed (see figure S6). Hence, for the quantification of the [S]/[Sn] ratio using Raman spectroscopy, only samples deposited at the temperature range between 380 – 430 °C were chosen. The composition of the selected samples were measured by WDX, and the [S]/[Sn] ratio are indicated in figure 6a. It was found that all deposited thin films are Sn-poor and the amount of S decreases with increasing substrate temperature or at further distances from the SnS precursor powders. These CVT samples deposited in inert atmospheres corresponds well with the higher thermodynamic stability of SnS as compared to SnS_2 and Sn_2S_3 [56]. As is seen in the Raman spectra of the selected CVT thin films (figure 6a) with a higher [S]/[Sn] ratio (i.e. deposited at lower temperatures), peaks for SnS_2 and Sn_2S_3 secondary phase were detected. However, according to XRD analysis relatively small amount (< 10 %) of these secondary phases were found to be present in these samples (see Figure S6), and no significant influence of their presence is expected to the following results. Note, that the cubic π-SnS polymorph was not detectable from, neither the XRD or Raman analyses of these CVT grown SnS samples. Furthermore a clear (100) preferred orientation of the CVT grown α-SnS samples were observed in all the XRD diffractograms (figure S6b).

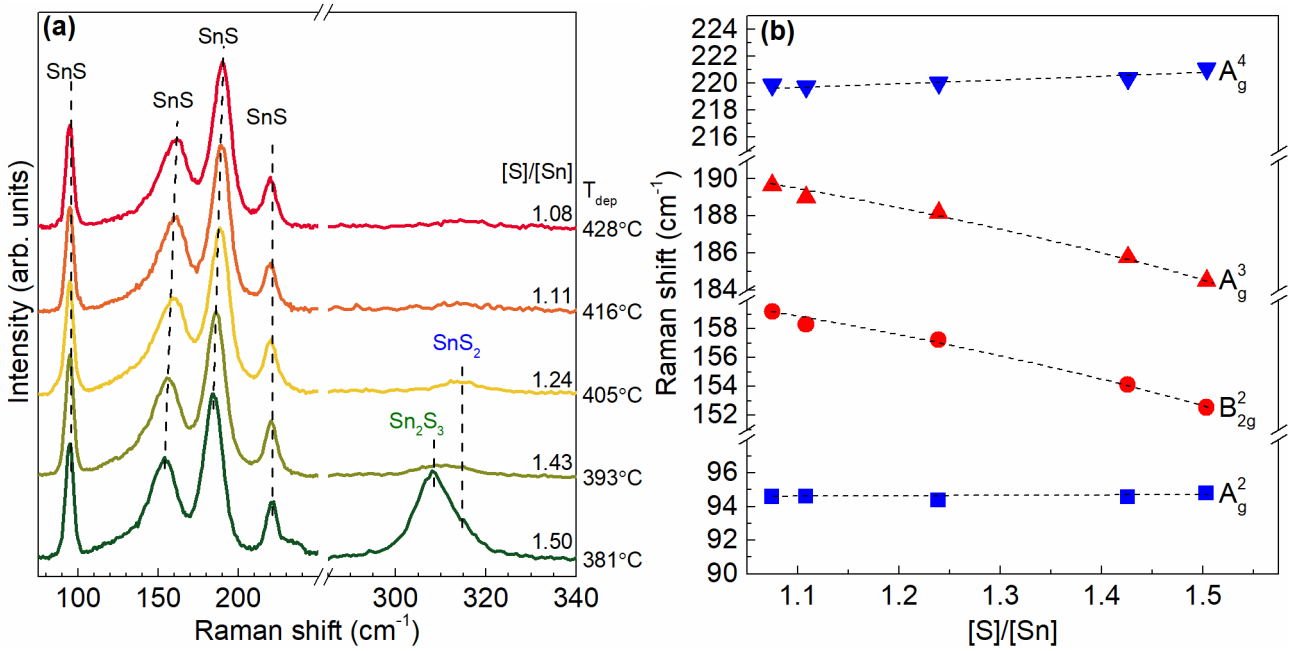

Figure 6. *(a) Raman spectra of glass/α-SnS samples deposited by CVT methods excited with 532 nm laser line. (b) Plot of Raman peaks positions as a function of the thin film composition/substrate deposition temperature. The errors do not exceed the spot size.*

As it was expected, for the CVT grown α-SnS samples, the correlated dependence of the relative Raman peak positions with the [S]/[Sn] ratio is maintained (figure 6b). As the thin film composition tends to stoichiometric SnS, the two intense A_g^3 and B_{2g}^2 Raman modes shift to higher frequencies while the other two (A_g^2 and A_g^4) almost remain in the same position. Hence, using these observations, a methodology for the quantitative assessment of the SnS composition by Raman spectroscopy has been developed. First a simple correlation between the position of certain modes with the composition were drawn (figure 6b), but in order to improve the accuracy of our method and to reduce the error and dependence on the peaks fitting process, we based our methodology on the relative shift of different Raman modes $\Delta\omega$. This parameter is defined as follows:

$$\Delta\omega = \left[2\omega\left(A_g^4\right) - \left(\omega\left(A_g^3\right) + \omega\left(B_{2g}^2\right)\right)\right]/2 \qquad (3)$$

where ω(X) corresponds to the relative shift of the Raman peak with X symmetry in cm^{-1}. The correlation between $\Delta\omega$ and sample composition is presented in figure 7 (dark yellow spheres), and a quadratic dependence of the $\Delta\omega$ parameter from the [S]/[Sn] ratio was observed. In order to increase the analysed compositional range, $\Delta\omega$ was calculated from the previously published Raman spectra [53] and the results were added to the same graph. As result, a similar dependence was

observed down to the [S]/[Sn] = 0.8, however a discrepancy of the two dependences was found. This is attributed to the accuracy in the evaluation of strict S and Sn content, and to the methodology used for the quantity calibration. In the Ref. [53] X-ray fluorescence (XRF) elemental analysis was used for this purpose, while WDX, used in the present study, offers higher resolution of quantitative chemical analysis. The former method is known to be less sensitive to the light atoms, like sulphur, and strongly dependent on the calibration samples. Thus a slight overestimation of S content in thin films of Ref. [53] can be a reason of the observed discrepancies between two dependencies in figure 7. Nevertheless, it is evident the possible use of proposed methodology of analysing the relative shift of different Raman modes to estimate [S]/[Sn] ratio. This way, to obtain strict equations describing the dependencies a set of reference samples should be analysed, where composition was measured with a high precision. Nevertheless, assuming a negligible error in the composition estimation in the present study the following quadratic equation can be proposed for the [S]/[Sn] ratio estimation:

$$[S]/[Sn] = -15.01 + 6.08 \times 10^{-1}\Delta\omega - 5.58 \times 10^{-3}\Delta\omega^2;\ (R^2 = 0.997). \quad (4)$$

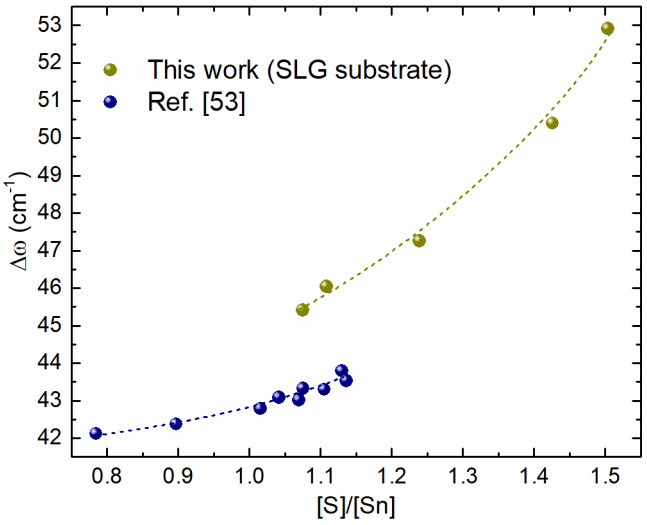

Figure 7. *Dependence of relative position of the Raman peaks (Δω) from the [S]/[Sn] ratio. The errors do not exceed the spot size.*

3.4 Decoupling the composition and secondary phase formation in SnS samples

In the past years different authors published their results on controlling the [S]/[Sn] ratio in the SnS layers by changing the deposition temperature [53,57-60] or applying post-deposition annealing [53,61,62]. Both effects lead to a strong change in the fundamental properties of the SnS compound [53,57-62], mostly explained by the influence of intrinsic point defects which are directly

related to the [S]/[Sn] ratio. Additionally, a direct influence of the [S]/[Sn] ratio was observed to the performance of the devices based on SnS, either for the efficiency of solar cells [53,57] or to improve the Seebeck coefficient in thermoelectric devices [60]. However, in a row with [S]/[Sn] ratio changing in SnS layers with deposition or annealing temperature, appearance of other compositional polymorphs of Sn-S system (SnS_2 or Sn_2S_3) are usually mentioned by the authors [53,57-61], and was also observed in the present study (see Sections 3.2 and 3.3). In this case most of the standard techniques applied for the [S]/[Sn] ratio estimation fail in determining this critical value strictly in SnS phase and only the overall ratio in the layer, combining the results from different phases, can be calculated. Moreover, a Sn or S content substrates, like FTO substrate used for the samples in Section 3.2, will influence most of the X-ray based techniques for the composition estimation. In this way, the methodology based on Raman scattering spectroscopy, proposed above, has a significant advantage, by providing the information not only about the phase content, but also about the exact value of [S]/[Sn] ratio in SnS phase of the thin film.

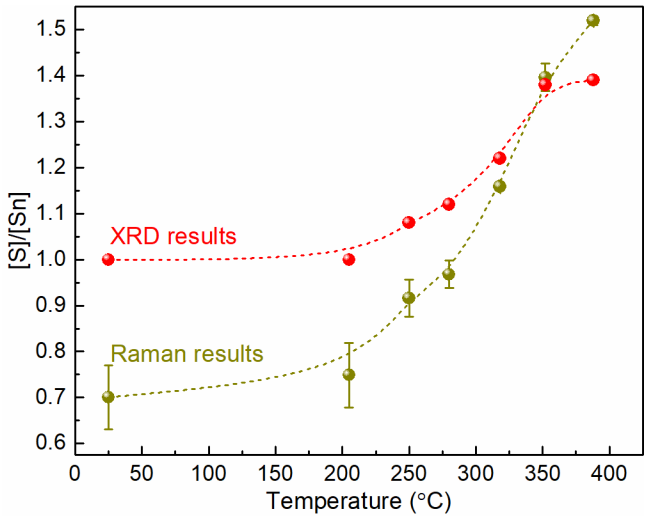

Figure 8. *[S]/[Sn] ratio for the α-SnS thin films annealed at different temperatures estimated from Raman spectroscopy and XRD analysis (see text for the details).*

To illustrate the application of the methodology proposed above, the Eq. (4) was applied to calculate the [S]/[Sn] ratio in the α-SnS films annealed at different temperatures analysed in the Section 3.2. As it seen, from figure 8 the un-annealed thin films are Sn-rich, while with increasing the annealing temperature they pass through the stoichiometric point and tends towards a strong S-rich composition. Note, that the error bars were calculated taking into account the standard

deviations for the terms in Eq. (4), and increasing of the uncertainty in the [S]/[Sn] ratio value with departure from the stoichiometric composition of the SnS was found. The overall [S]/[Sn] ratio in the figure 8 was estimated using the data of phase concentration obtained in the XRD analysis (see Table S1), and considering the stoichiometric composition of each presented phase. As result a large difference between the overall [S]/[Sn] ratio in the SnS polymorphs were observed. The application of the Raman based methodologies for the evaluation of the SnS layers has a strong potential allowing for the identification and quantification the [S]/[Sn] ratio, which is known to be strongly linked to the concentration of intrinsic defects. Independence of the Raman based methodology from the substrate and from the phase content can provide a more detailed information for the understanding the fundamental materials limitation and a more strict dependences of the optoelectronic properties from the layer composition.

4. Conclusion

This work presents a complete report of vibrational properties for SnS structural polymorphs. First, both α- and π-SnS polymorphs were characterized by Raman spectroscopy using several excitation wavelengths and resonant behaviours were brought into light. These resonant phenomena are due to the coupling of the excitation energy used with certain band to band transitions in the α-SnS and π-SnS band diagrams. The spectra for the π-SnS thin film samples were measured down to the lower frequency region comparing to the previously reported experimental data, while in the case of α-SnS more strict position of the peaks in the experimental Raman spectra was determined. A strong correlation of the position of the certain Raman modes with stoichiometric deviations was observed for the α-polymorph: an increase in the [S]/[Sn] ratio (i.e. loss of Sn) induced a red shift of A_g^3 and B_{2g}^2 Raman modes towards lower frequencies. As a consequence, close monitoring of the relative peak positions for these Raman modes was proposed as methodology for assessment of the small compositional changes in α-SnS polymorph. Moreover, an in-depth investigation of the mild temperature annealing of α-SnS revealed that even with these conditions it was possible to alter the composition of SnS samples. The potential of the Raman and XRD combined analysis has been evaluated in order to develop a methodology for a more accurate description of the system. The application of both techniques provides a tool to spatially map the stoichiometry and composition of α-SnS thin film samples.

Acknowledgements

This research was supported by the H2020 Programme under the project INFINITE-CELL (H2020-MSCA-RISE-2017-777968), by the Spanish Ministry of Science, Innovation and Universities under the WINCOST (ENE2016-80788-C5-1-R), and by the European Regional Development Funds (ERDF, FEDER Programa Competitivitat de Catalunya 2007–2013). Authors from IREC and the University of Barcelona belong to the SEMS (Solar Energy Materials and Systems) Consolidated Research Group of the "Generalitat de Catalunya" (Ref. 2017 SGR 862). M.P. thanks the Government of Spain for the Ramon y Cajal Fellowship (RYC-2017-23758).

References

[1] T.D. Lee, A.U. Ebong, A review of thin film solar cell technologies and challenges, Renew. Sust. Energ. Revi. 70 (2017) 1286-1297.

[2] S. Giraldo, Z. Jehl, M. Placidi, V. Izquierdo- Roca, A. Pérez- Rodríguez, E. Saucedo, Progress and perspectives of thin film kesterite photovoltaic technology: A critical review, Adv. Mater. 31 (2019) 1806692.

[3] V.R.M. Reddy, M.R. Pallavolu, P.R. Guddeti, S. Gedia, K.K.Y.B. Reddy, B. Pejjaia, W.K. Kim, T.R.R. Kotte, C. Park, Review on Cu_2SnS_3, Cu_3SnS_4, and Cu_4SnS_4 thin films and their photovoltaic performance, J. Ind. Eng. Chem. 76 (2019) 39-74.

[4] J.A. Andrade-Arvizu, M. Courel-Piedrahita, O. Vigil-Galan, SnS-based thin film solar cells: perspectives over the last 25 years, J. Mater. Sci.: Mater. El. 26 (2015) 4541-4556.

[5] P. Sinsermsuksakul, L. Sun, S.W. Lee, H.H. Park, S.B. Kim, C. Yang, R.G. Gordon, Overcoming efficiency limitations of SnS- based solar cells, Adv. Energy Mater. 4 (2014) 1400496.

[6] L.A. Burton, D. Colombara, R.D. Abellon, F.C. Grozema, L.M. Peter, T.J. Savenije, G. Dennler, A. Walsh, Synthesis, characterization, and electronic structure of single-crystal SnS, Sn_2S_3, and SnS_2, Chem. Mater. 25 (2013) 4908-4916.

[7] H.- S. Yun, B.- w. Park, Y.C. Choi, J. Im, T.J. Shin, S.I. Seok, Efficient nanostructured TiO_2/SnS heterojunction solar cells, Adv. Energy Mater. 9 (2019) 1901343.

[8] W. Guang-Pu, Z. Zhi-Lin, Z. Wei-Ming, G. Xiang-Hong, C. Wei-Qun, H. Tanamura, M. Yamaguchi, H. Noguchi, T. Nagatomo, O. Omoto, Proceedings of 1994 IEEE 1st World Conference on Photovoltaic Energy Conversion – WCPEC 1 (1994) 365-368.

[9] Y. Iguchi, K. Inoue, T. Sugiyama, H. Yanagi, Single-crystal growth of Cl-doped n-type SnS using $SnCl_2$ self-flux, Inorg. Chem. 57 (2018) 6769-6772.

[10] B. Ghosh, R. Bhattacharjee, P. Banerjee, S. Das, Structural and optoelectronic properties of vacuum evaporated SnS thin films annealed in argon ambient, Appl. Surf. Sci. 257 (2011) 3670-3676.

[11] E.E. Matyas, System PbTe-SnS, Inorg. Mater. (Engl. Transl.) 21 (1985) 124.

[12] P. Kevin, D.J. Lewis, J. Raftery, M.M. Azad, P. O'Brien, Thin films of tin(II) sulphide (SnS) by aerosol-assisted chemical vapour deposition (AACVD) using tin(II) dithiocarbamates as single-source precursors, J. Cryst. Growth 415 (2015) 93-99.

[13] A. de Kergommeaux, M. Lopez-Haro, S. Pouget, J.-M. Zuo, C. Lebrun, F. Chandezon, D. Aldakov, P. Reiss, Synthesis, internal structure, and formation mechanism of monodisperse tin sulfide nanoplatelets, J. Amer. Chem. Soc. 137 (2015) 9943-9952.

[14] I.Y. Ahmet, M.S. Hill, A.L. Johnson, L.M. Peter, Polymorph-selective deposition of high purity SnS thin films from a single source precursor, Chem. Mater. 27 (2015) 7680-7688.

[15] Z. Deng, D. Han, Y. Liu, Colloidal synthesis of metastable zinc-blende IV-VI SnS nanocrystals with tunable sizes, Nanoscale 3 (2011) 4346-4351.

[16] W. Guo, Y. Shen, M. Wu, T. Ma, Highly efficient inorganic-organic heterojunction solar cells based on SnS-sensitized spherical TiO_2 electrodes, Chem. Commun. 48 (2012) 6133-6135.

[17] A. Rabkin, S. Samuha, R.E. Abutbul, V. Ezersky, L. Meshi, Y. Golan, New nanocrystalline materials: a previously unknown simple cubic phase in the SnS binary system, Nano Lett. 15 (2015) 2174-2179.

[18] R.E. Abutbul, A.R. Garcia-Angelmo, Z. Burshtein, M.T.S. Nair, P.K. Nair, Y. Golan, Crystal structure of a large cubic tin monosulfide polymorph: an unraveled puzzle, CrystEngComm 18 (2016) 5188-5194.

[19] A.R. Garcia-Angelmo,; R.; Romano-Trujillo, J.; Campos-Álvarez, O.; Gomez-Daza, M. T. S.; Nair, P. K. Nair, Thin film solar cell of SnS absorber with cubic crystalline structure, Phys. Stat. Solidi A 212 (2015) 2332-2340.

[20] I.Y. Ahmet, M. Guc, Y. Sánchez, M. Neuschitzer, V. Izquierdo-Roca, E. Saucedo, A.L. Johnson, Evaluation of AA-CVD deposited phase pure polymorphs of SnS for thin films solar cells, RSC Adv. 9 (2019) 14899-14909.

[21] S. Schorr, G. Gurieva, M. Guc, M. Dimitrievska, A. Pérez-Rodríguez, V. Izquierdo-Roca, C.S. Schnohr, J. Kim, W. Jo, J.M. Merino, Point defects, compositional fluctuations and secondary phases in non-stoichiometric kesterites. J. Phys. Energy (2019). https://doi.org/10.1088/2515-7655/ab4a25

[22] F. Oliva, L. Arqués, L. Acebo, M. Guc, Y. Sánchez, X. Alcobé, A. Perez-Rodriguez, E. Saucedo, V. Izquierdo-Roca, Characterization of Cu_2SnS_3 polymorphism and its impact on optoelectronic properties, J. Mater. Chem. A 5 (2017) 23863-23871.

[23] M. Dimitrievska, F. Oliva, M. Guc, S. Giraldo, E. Saucedo, A. Pérez-Rodríguez, V. Izquierdo-Roca, Defect characterisation in $Cu_2ZnSnSe_4$ kesterites via resonance Raman spectroscopy and the impact on optoelectronic solar cell properties, J. Mater. Chem. A 7 (2019) 13293-13304.

[24] M. Guc, F. Oliva, R. Kondrotas, X. Alcobe, M. Placidi, P. Pistor, E. Saucedo, A. Perez- Rodriguez, V. Izquierdo- Roca, $CuZnInSe_3$- based solar cells: Impact of copper concentration on vibrational and structural properties and device performance, Prog. Photovoltaics 27 (2019) 716-723.

[25] F. Oliva, S. Kretzschmar, D. Colombara, S. Tombolato, C. Maria Ruiz, A. Redinger, E. Saucedo, C. Broussillou, T. Goislardde Monsabert, T. Unold, P.J. Dale, V. Izquierdo-Roca, A. Pérez-Rodríguez, Optical methodology for process monitoring of chalcopyrite photovoltaic technologies: Application to low cost $Cu(In,Ga)(S,Se)_2$ electrodeposition based processes, Sol. Energy Mater. Sol. Cell 158 (2016) 168-183.

[26] M. Guc, D. Hariskos, L. Calvo-Barrio, P. Jackson, F. Oliva, P. Pistor, A. Perez-Rodriguez, V. Izquierdo-Roca, Resonant Raman scattering based approaches for the quantitative assessment of nanometric ZnMgO layers in high efficiency chalcogenide solar cells. Sci. Rep. 7 (2017) 1144.

[27] C. Insignares-Cuello, X. Fontané, Y. Sánchez-González, M. Placidi, C. Broussillou, J. López-García, E. Saucedo, V. Bermúdez, A. Pérez-Rodríguez, V. Izquierdo-Roca, Non-destructive assessment of ZnO:Al window layers in advanced $Cu(In,Ga)Se_2$ photovoltaic technologies, Phys. Status Solidi A 212 (2015) 56-60.

[28] M. Guc, F. Tsin, J. Rousset, Y.E. Romanyuk, V. Izquierdo-Roca, A. Pérez-Rodríguez, Non-destructive Raman scattering assessment of solution-processed ZnO doped layers for photovoltaic applications, J. Phys. Chem. C 121 (2017) 3212-3218.

[29] M. Dimitrievska, A. Fairbrother, X. Fontané, T. Jawhari, V. Izquierdo-Roca, E. Saucedo, A. Pérez-Rodríguez, Multiwavelength excitation Raman scattering study of polycrystalline kesterite Cu_2ZnSnS_4 thin films, Appl. Phys. Lett. 104 (2014) 021901.

[30] D. Nam, J.-U. Lee, H. Cheong, Excitation energy dependent Raman spectrum of $MoSe_2$, Sci. Rep. 5 (2015) 17113.

[31] M. Placidi, M. Dimitrievska, V. Izquierdo-Roca, X. Fontané, A. Castellanos-Gomez, A. Pérez-Tomás, N. Mestres, M. Espindola-Rodriguez, S. López-Marino, M. Neuschitzer, V. Bermudez, A. Yaremko, A. Pérez-Rodríguez, Multiwavelength excitation Raman scattering analysis of bulk and two-dimensional MoS_2: vibrational properties of atomically thin MoS_2 layers, 2D Mater. 2 (2015) 035006.

[32] E. Garcia-Llamas, M. Guc, I.V. Bodnar, X. Fontané, R. Caballero, J.M. Merino, M. León, V. Izquierdo-Roca, Multiwavelength excitation Raman scattering of Cu2ZnSn1-xGex(S,Se)4 single crystals for earth abundant photovoltaic applications, J. Alloy Compd. 692 (2017) 249-256.

[33] P. Vidal-Fuentes, M. Guc, X. Alcobe, A. Pérez-Rodríguez, E. Saucedo, V. Izquierdo-Roca, Multiwavelength excitation Raman scattering study of Sb_2Se_3 compound: fundamental vibrational properties and secondary phases detection, 2D Mater. 6 (2019) 045054.

[34] J.M. Skelton, L.A. Burton, A.J. Jackson, F. Oba, S.C. Parker, A. Walsh, Lattice dynamics of the tin sulphides SnS_2, SnS and Sn_2S_3: vibrational spectra and thermal transport, Phys. Chem. Chem. Phys. 19 (2017) 12452-12465.

[35] M. Li, Y. Zhu, T. Li, Y. Lin, H. Cai, S. Li, H. Ding, N. Pan, X. Wang, One-step CVD fabrication and optoelectronic properties of SnS2/SnS vertical heterostructures, Inorg. Chem. Front. 5 (2018) 1828-1835.

[36] M. Li, Y. Wu, T. Li, Y. Chen, H. Ding, Y. Lin, N. Pan, X. Wang, Revealing anisotropy and thickness dependence of Raman spectra for SnS flakes, RSC Adv. 7 (2017) 48759-48765.

[37] S. Di Mare, D. Menossi, A. Salavei, E. Artegiani, F. Piccinelli, A. Kumar, G. Mariotto, A. Romeo, SnS thin film solar cells: perspectives and limitations, Coatings 7 (2017) 34.

[38] R.E. Abutbul, E. Segev, L. Zeiri, V. Ezersky, G. Makov, Y. Golan, Synthesis and properties of nanocrystalline π-SnS – a new cubic phase of tin sulphide, RSC Adv. 6 (2016) 5848-5855.

[39] H. Rietveld, A profile refinement method for nuclear and magnetic structures, J. Appl. Cryst. 2 (1969) 65-71.

[40] D.L. Bish, S.A. Howard, Quantitative analysis using the Rietveld method, J. Appl. Cryst. 21 (1988) 86-91.

[41] A. Coelho, J. Evans, I. Evans, A. Kern, S. Parsons, The TOPAS symbolic computation system, Powder Diffr. 26 (2011) S22-S25.

[42] Bruker AXS, TOPAS, v5.0 (Computer Software), Karslruhe, Germany (2011).

[43] R. Cheary, A. Coelho, J. Cline, Fundamental parameters line profile fitting in laboratory diffractometers. J. Res. Natl. Inst. Stan. 109 (2004) 1-25.

[44] H. Seki, N. Ishizawa, N. Mizutani, M. Kato, K. Yogyo, High-temperature structures of the rutile-type oxides, TiO_2 and SnO_2, J. Ceram. Assoc. Jpn. 92 (1984) 219.

[45] R.M. Hazen, L.W. Finger, The crystal structures and compressibilities of layer minerals at high pressure. I. SnS_2, berndtite, Am. Mineral. 63 (1978) 289-292.

[46] D. Mootz, H. Puhl, Die Kristallstruktur von Sn_2S_3, Acta Crystallogr. 23 (1967) 471.

[47] A. Stokes, A. Wilson, A method of calculating the integral breadths of Debye-Scherrer lines, Math. Proc. Cambridge 38 (1942) 313-322.

[48] P.M. Nikolic, P. Mihajlovic, B. Lavrencic, Splitting and coupling of lattice modes in the layer compound SnS, J. Phys. C: Solid State Phys. 10 (1977) L289.

[49] H. R. Chandrasekhar, R. G. Humphreys, U. Zwick, M. Cardona, Infrared and Raman spectra of the IV-VI compounds SnS and SnSe, Phys. Rev. B 15 (1977) 2177.

[50] R.E. Banai, L.A. Burton, S.G. Choi, F. Hofherr, T. Sorgenfrei, A. Walsh, B. To, A. Croll, J. R. S. Brownson, Ellipsometric characterization and density-functional theory analysis of anisotropic optical properties of single-crystal α-SnS, J. Appl. Phys. 116 (2014) 013511.

[51] M. Dimitrievska, H. Xie, A. J. Jackson, X. Fontané, M. Espíndola-Rodríguez, E. Saucedo, A. Pérez-Rodríguez, A. Walsh, V. Izquierdo-Roca, Resonant Raman scattering of ZnS_xSe_{1-x} solid solutions: the role of S and Se electronic states, Phys. Chem. Chem. Phys. 18 (2016) 7632-7640.

[52] J. Vidal, S. Lany, Mayeul d'Avezac, A. Zunger, A. Zakutayev, J. Francis, J. Tate, Band-structure, optical properties, and defect physics of the photovoltaic semiconductor SnS, Appl. Phys. Lett. 100 (2012) 032104.

[53] A. Yago, T. Kibishi, Y. Akaki, S. Nakamura, H. Oomae, H. Katagiri, H. Araki, Influence of Sn/S composition ratio on SnS thin-film solar cells produced via co-evaporation method, Jpn. J. Appl. Phys. 57 (2018) 02CE08.

[54] J. Breternitz, R. Gunder, H. Hempel, S. Binet, I. Ahmet, S. Schorr, Facile bulk synthesis of π-cubic SnS, Inorg. Chem. 56 (2017) 11455-11457.

[55] A. Voznyi, V. Kosyak, P. Onufrijevs, L. Grase, J. Vecstaudža, A. Opanasyuk, A. Medvid, Laser-induced SnS_2-SnS phase transition and surface modification in SnS_2 thin films, J. Alloy Compd. 688 (2016) 130-139.

[56] L.A. Burton, A. Walsh, Phase Stability of the earth-abundant tin sulfides SnS, SnS_2, and Sn_2S_3, J. Phys. Chem. C 116 (2012) 24262-24267.

[57] Y. Kawano, J. Chantana, T. Minemoto, Impact of growth temperature on the properties of SnS film prepared by thermal evaporation and its photovoltaic performance, Curr. Appl. Phys. 15 (2015) 897-901.

[58] J.A. Andrade-Arvizu, M.F. García-Sánchez, M. Courel-Piedrahita, F. Pulgarín-Agudelo, E. Santiago-Jaimes, E. Valencia-Resendiz, A. Arce-Plaza, O. Vigil-Galán, Suited growth parameters inducing type of conductivity conversions on chemical spray pyrolysis synthesized SnS thin films, J. Anal. Appl. Pyrol. 121 (2016) 347-359.

[59] V.R.M. Reddy, S. Gedi, C. Park, R.W. Miles, R.R. K.T., Development of sulphurized SnS thin film solar cells, Curr. Appl. Phys. 15 (2015) 588-598.

[60] H. Zhang, Y. Balaji, A.N. Mehta, M. Heyns, M. Caymax, Iu. Radu, W. Vandervorst, A. Delabie, Formation mechanism of 2D SnS_2 and SnS by chemical vapor deposition using $SnCl_4$ and H_2S, J. Mater. Chem. C 6 (2018) 6172-6178.

[61] T.S. Reddy, B.H. Kumar, M.C.S. Kumar, Effect of annealing on the optical properties and photoconductivity of SnS thin film, AIP Conf. Proc. 1832 (2017) 080043.

[62] P. Jain, P. Arun, Influence of grain size on the band-gap of annealed SnS thin films, Thin Solid Films 548 (2013) 241-246.

Figures captions

Figure 1. Scheme presenting the two synthetises methods for the deposition of SnS thin film samples. (a) presents the selective deposition of homogeneous α- and π- SnS thin films using aerosol assisted chemical vapour deposition (AA-CVD) and (b) presents the chemical vapour transport (CVT) method resulting in a lateral gradient in the composition of α-SnS samples.

Figure 2. Rietveld refinement of an XRD pattern of (a) α-SnS and (b) π-SnS thin films deposited onto FTO coated soda-lime glass substrates.

Figure 3. Raman spectra, measured with different excitation wavelengths, for pure (a) α-SnS and (b) π-SnS thin film samples deposited by AA-CVD. The low intensity peaks in the high wavenumbers range are emphasized in the figure S1 from the Supporting Information.

Figure 4. Top – XRD pattern of (a) α-SnS and (b) π-SnS thin films annealed at different temperatures under air atmosphere for 10 min. Bottom – Raman spectra excited with 532 nm laser line of (c) α-SnS and (d) π-SnS thin films annealed at different temperatures under air atmosphere for 10 min.

Figure 5. (a) Shift of the main α-SnS Raman peaks positions versus different annealing temperatures. (b) Change of the lattice parameters of both SnS polymorphs versus different annealing temperatures. The errors in both graphs do not exceed the spot size.

Figure 6. (a) Raman spectra of glass/α-SnS samples deposited by CVT methods excited with 532 nm laser line. (b) Plot of Raman peaks positions as a function of the thin film composition/substrate deposition temperature. The errors do not exceed the spot size.

Figure 7. Dependence of relative position of the Raman peaks ($\Delta\omega$) from the [S]/[Sn] ratio. The errors do not exceed the spot size.

Figure 8. [S]/[Sn] ratio for the α-SnS thin films annealed at different temperatures estimated from Raman spectroscopy and XRD analysis (see text for the details).

Figure 1

Click here to download high resolution image

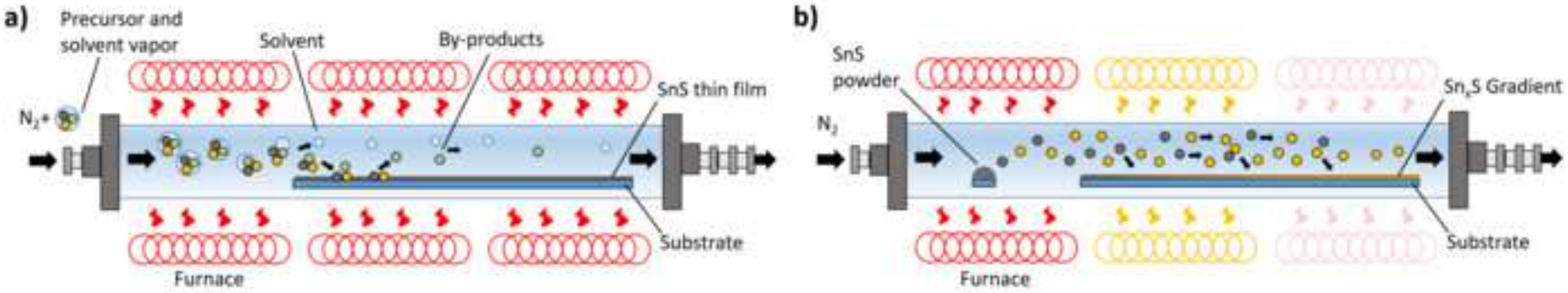

Figure 2a

Click here to download high resolution image

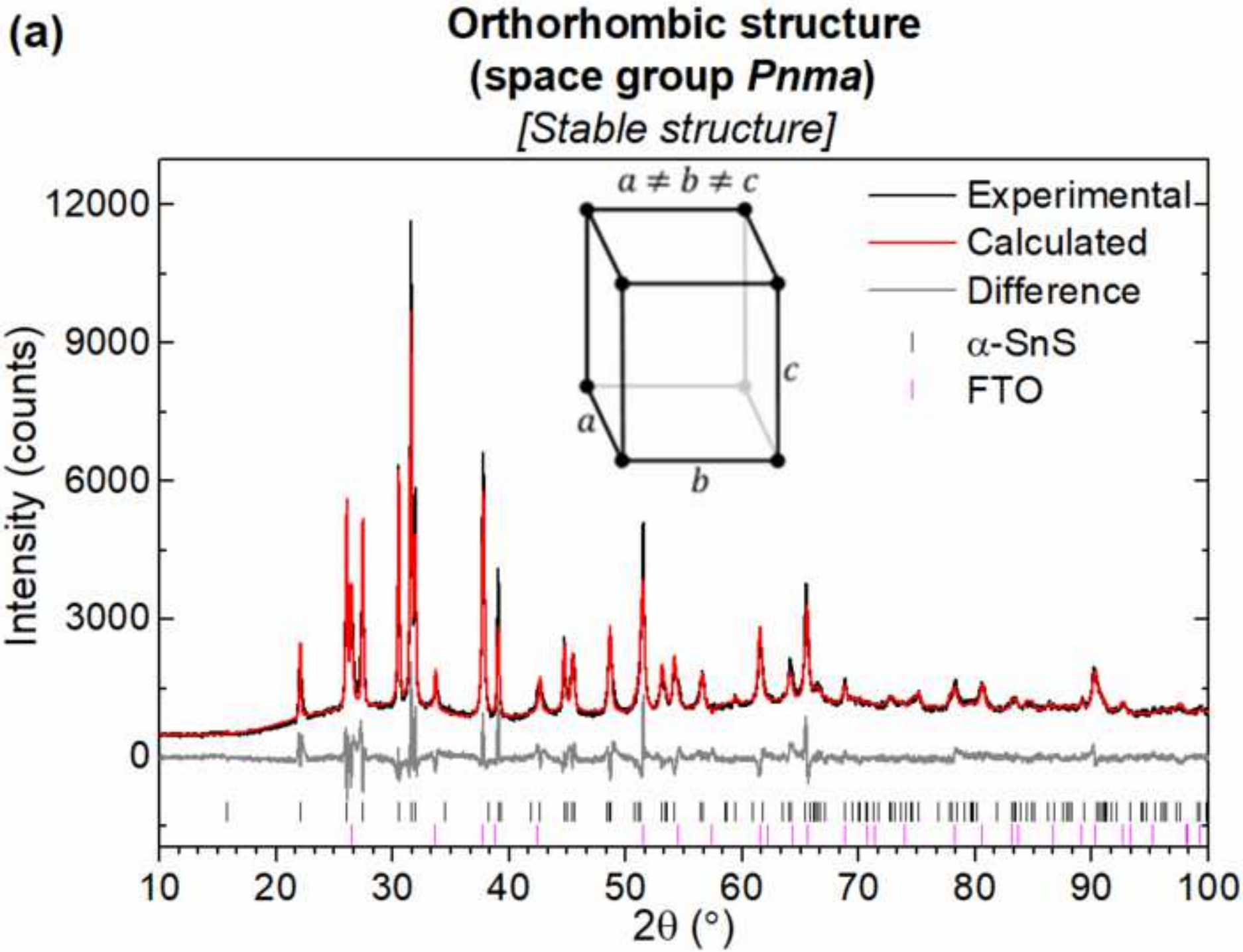

Figure 2b

Click here to download high resolution image

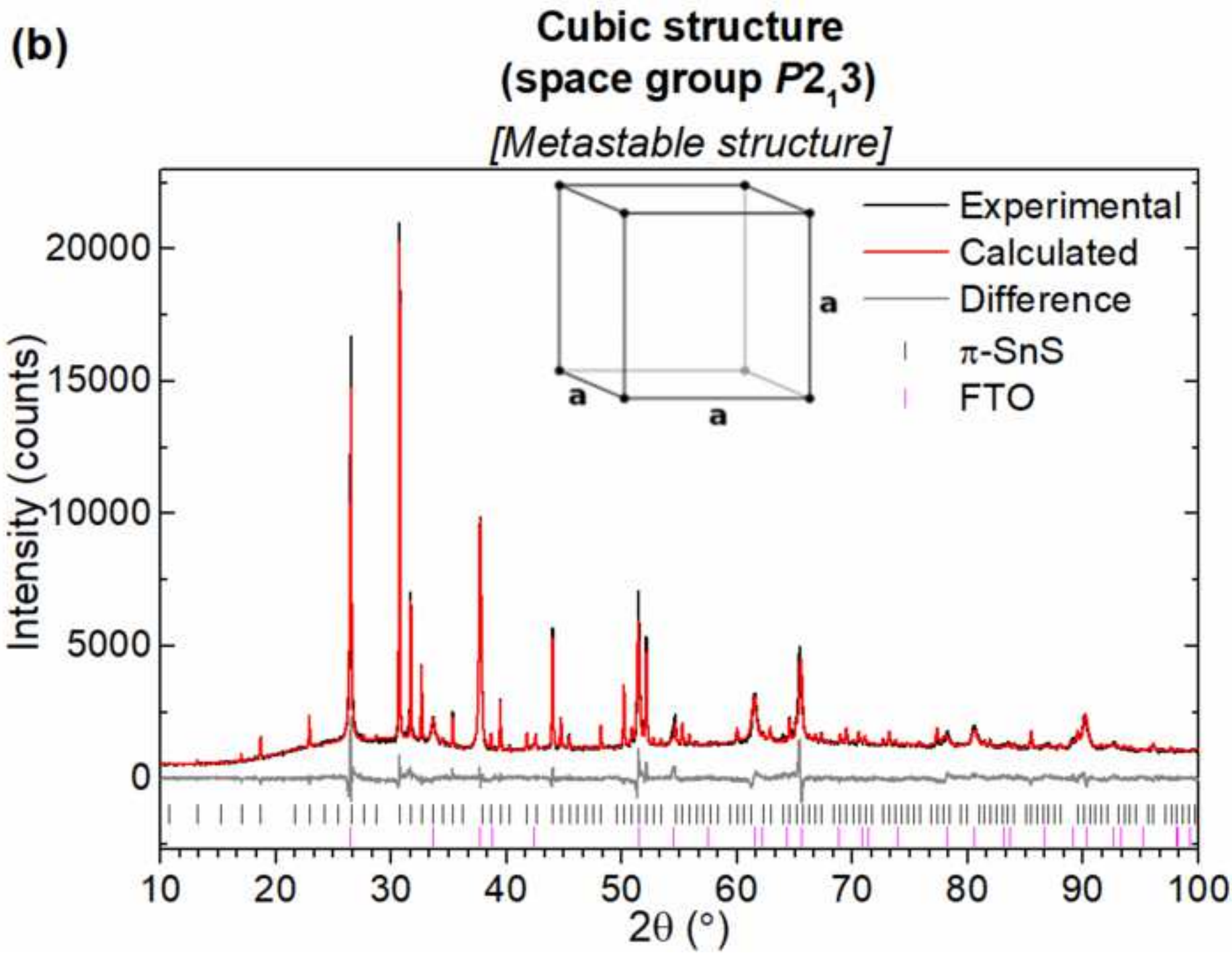

Figure 3a

Click here to download high resolution image

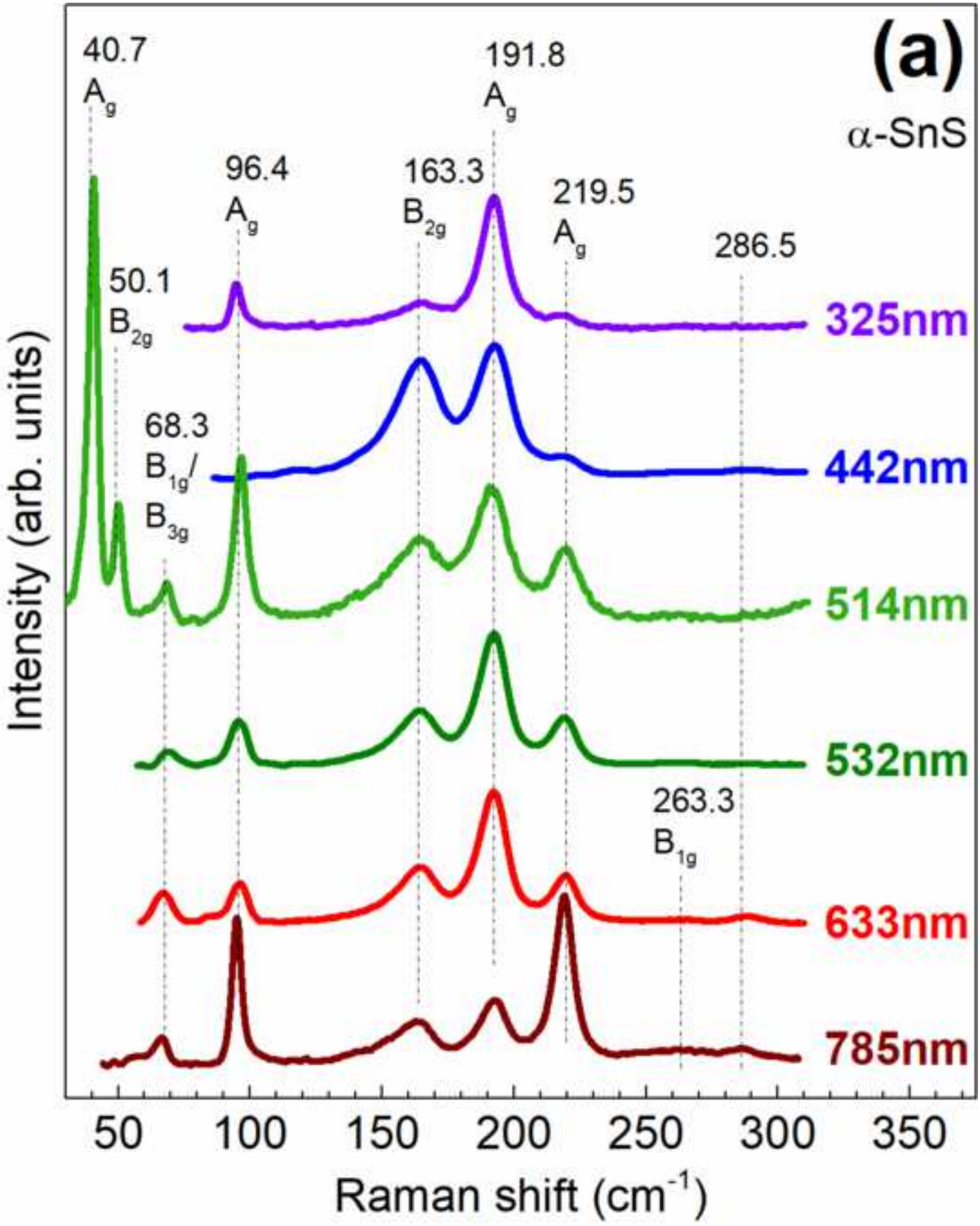

Figure 3b
Click here to download high resolution image

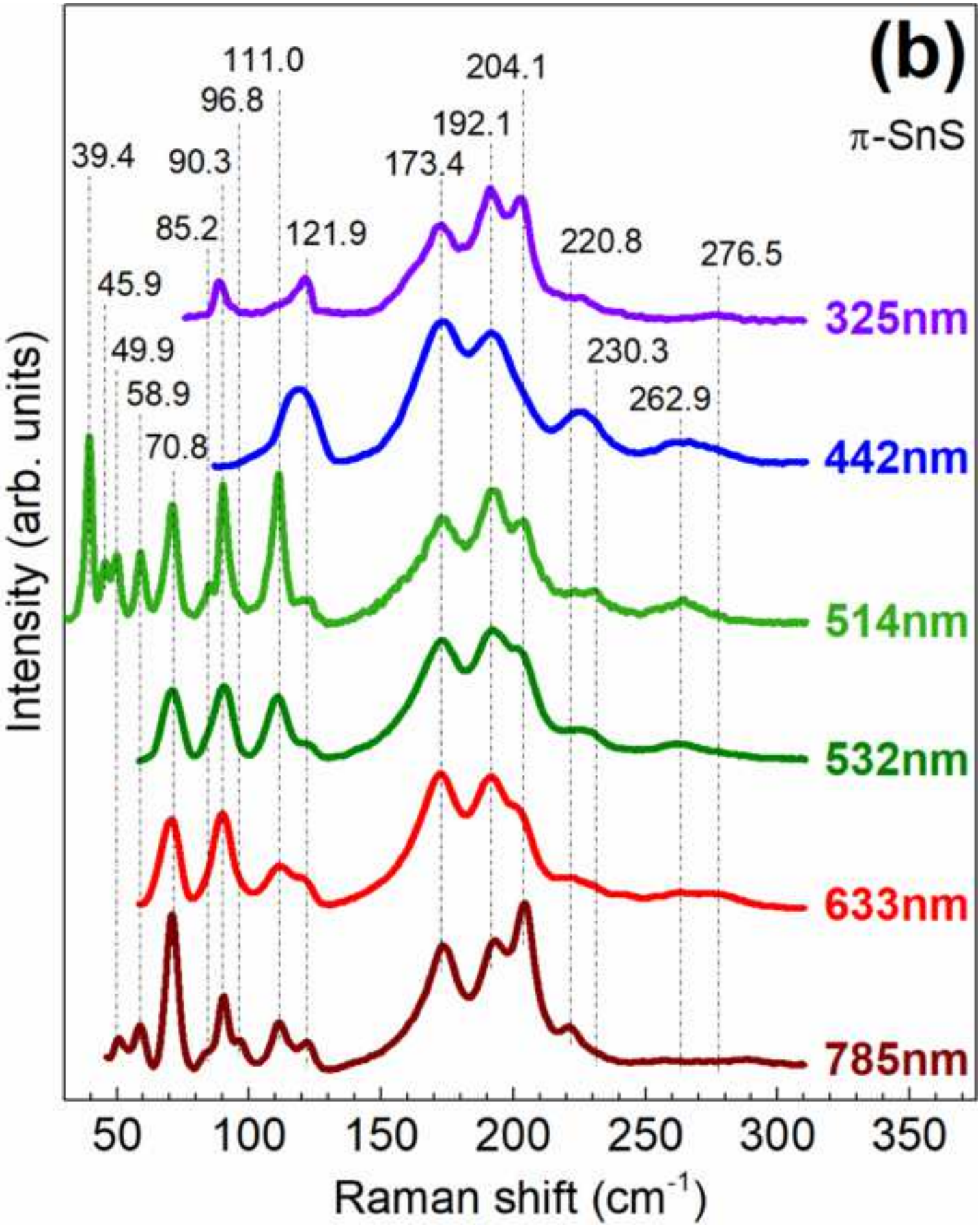

Figure 4a

Click here to download high resolution image

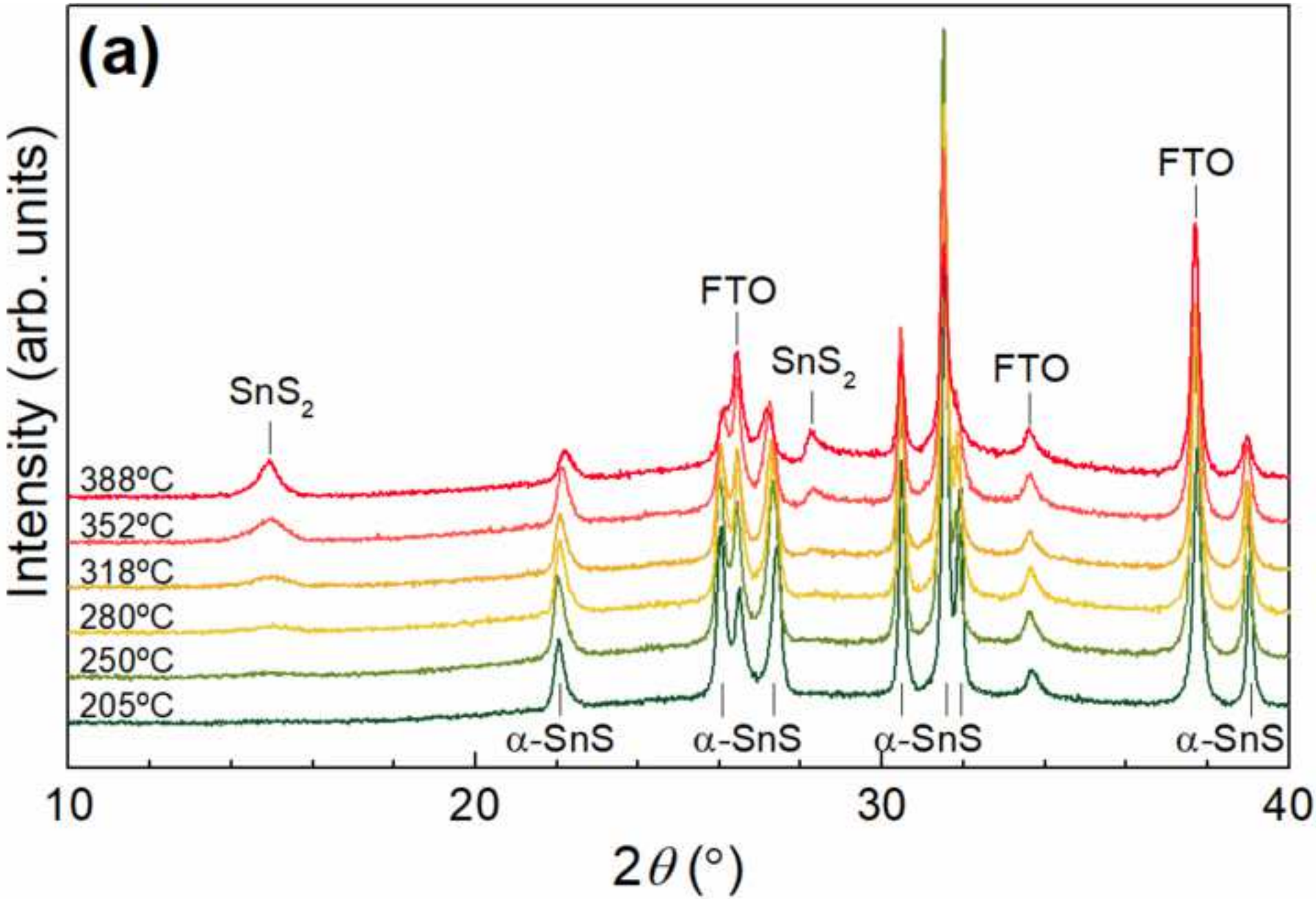

Figure 4b

Click here to download high resolution image

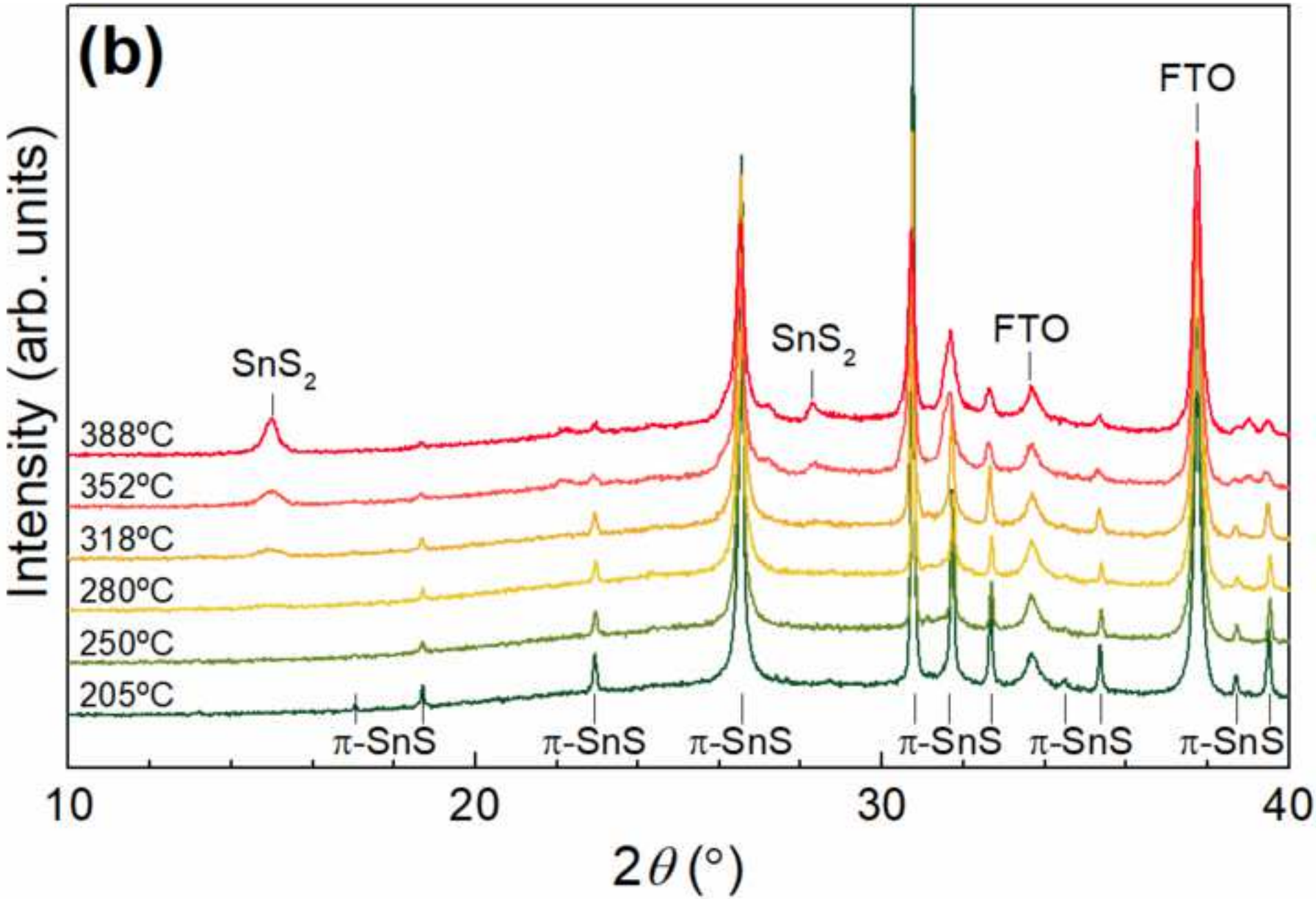

Figure 4c

Click here to download high resolution image

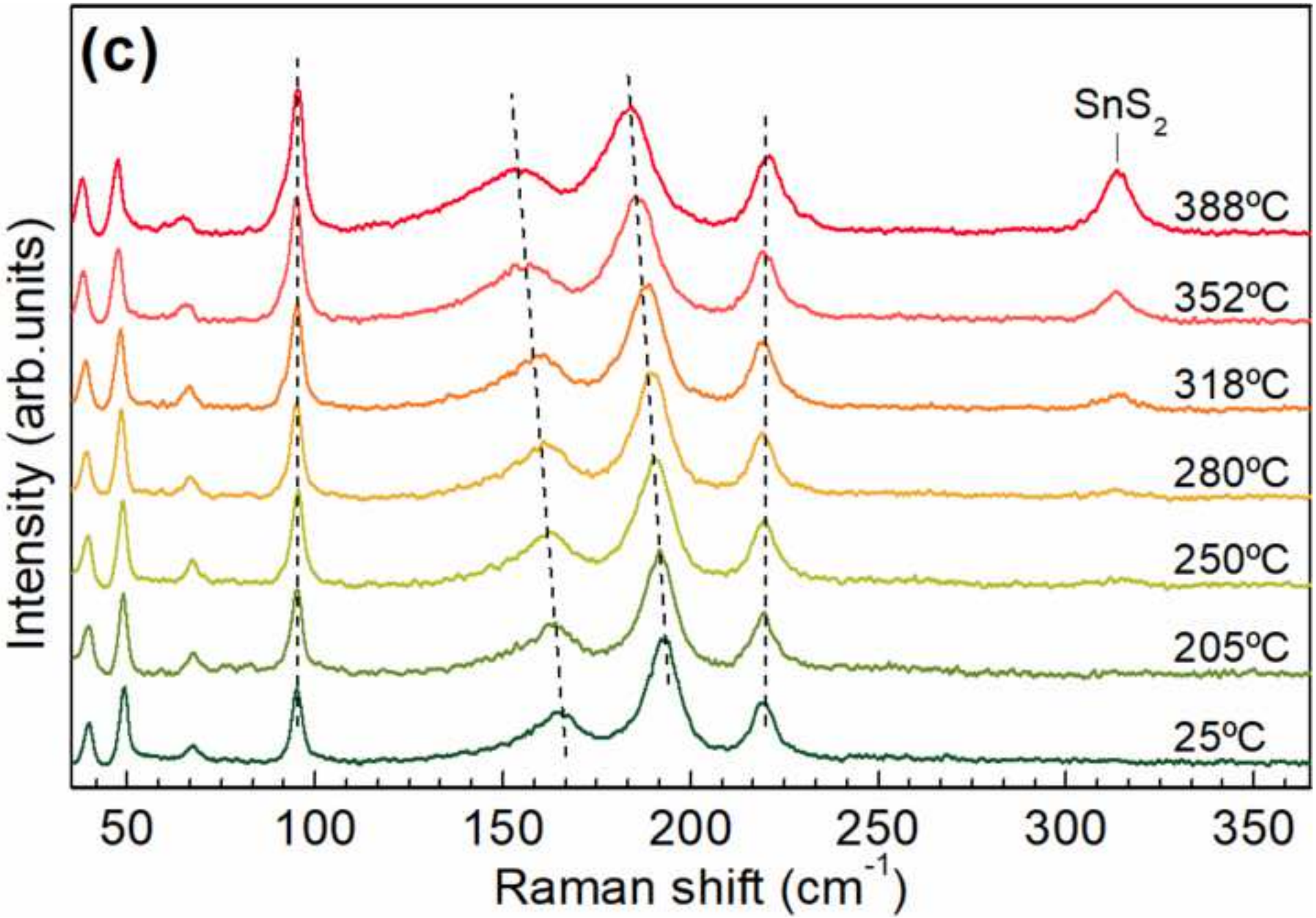

Figure 4d
Click here to download high resolution image

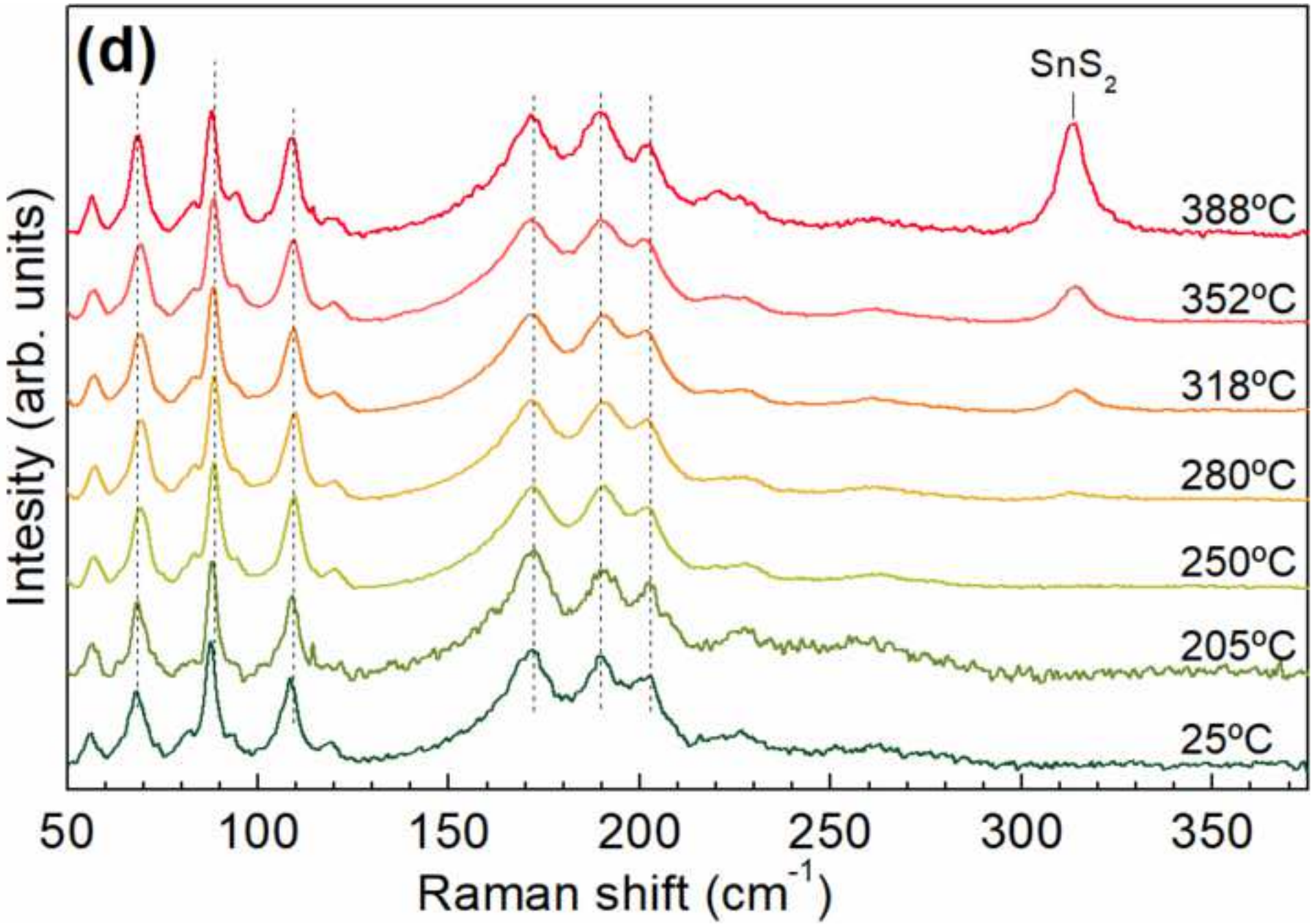

Figure 5a

Click here to download high resolution image

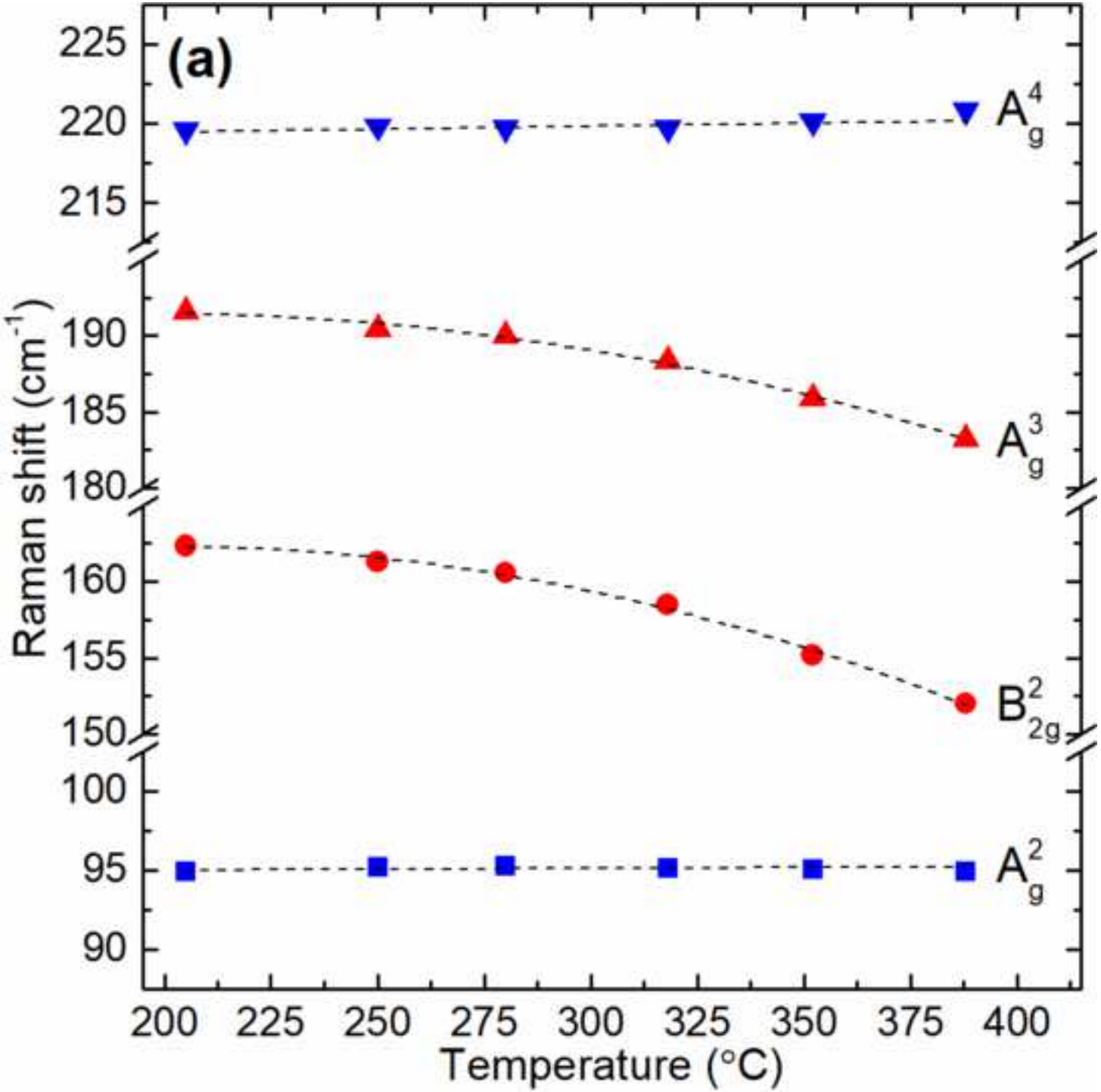

Figure 5b

Click here to download high resolution image

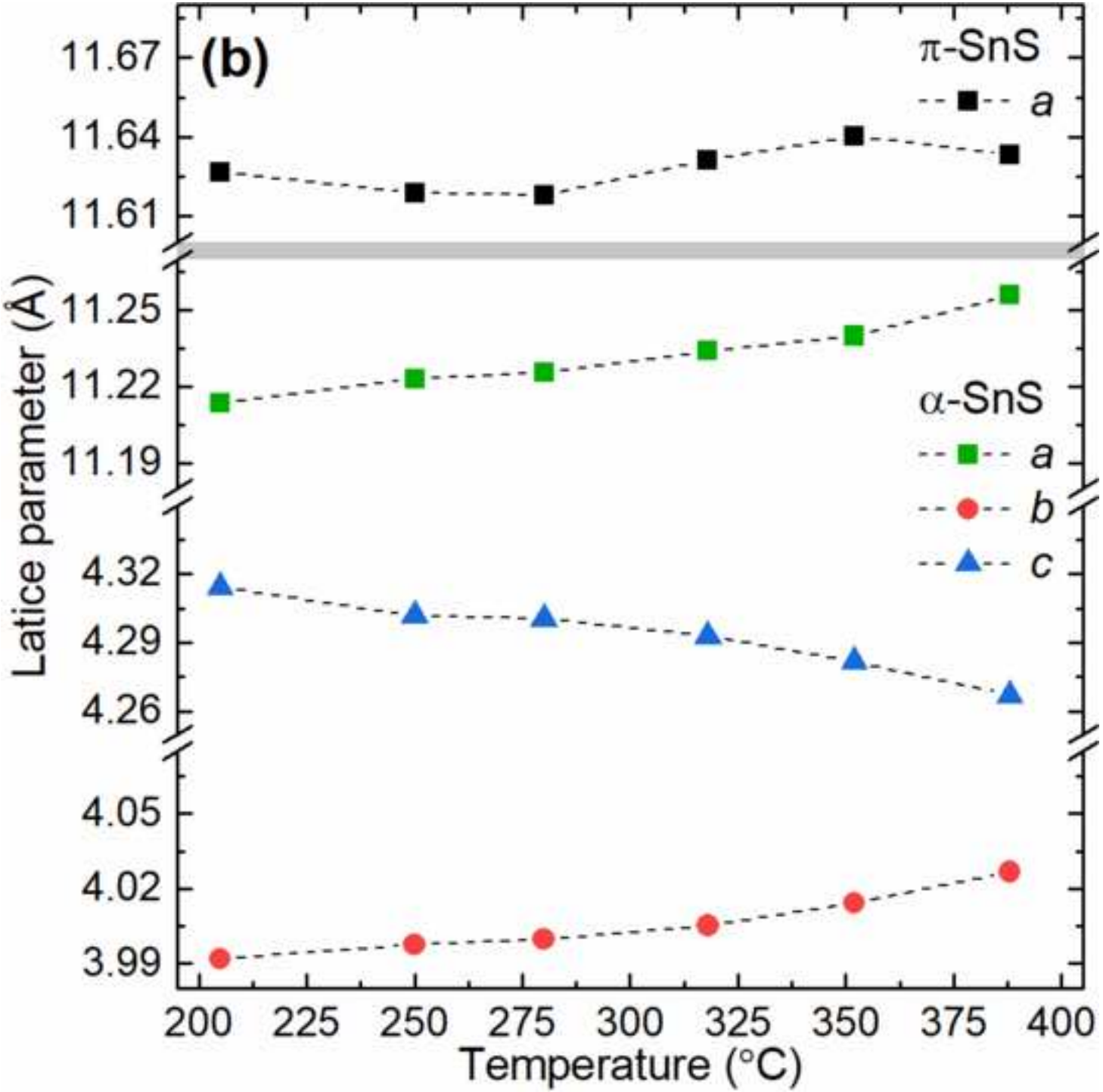

Figure 6a

Click here to download high resolution image

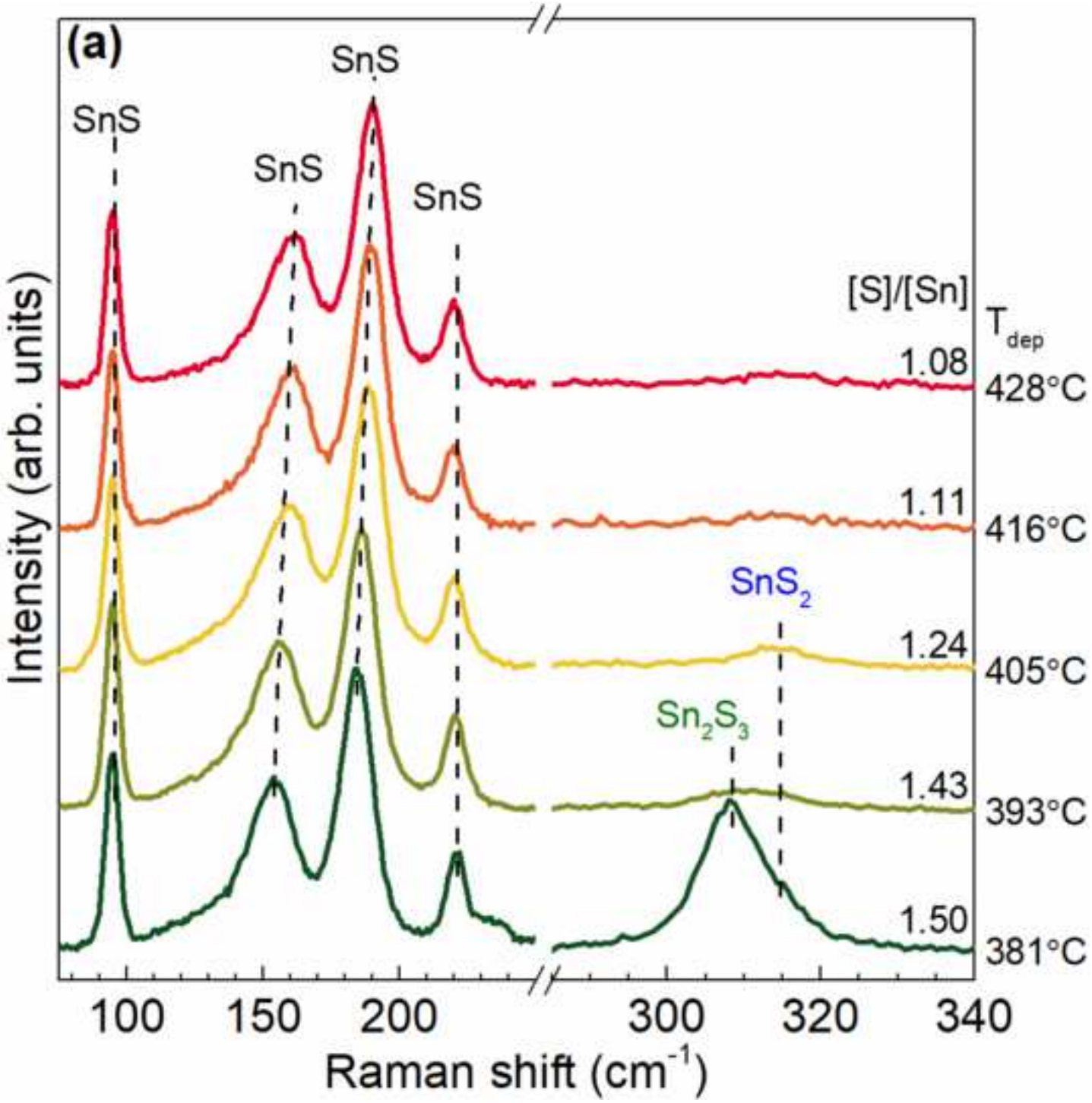

Figure 6b

Click here to download high resolution image

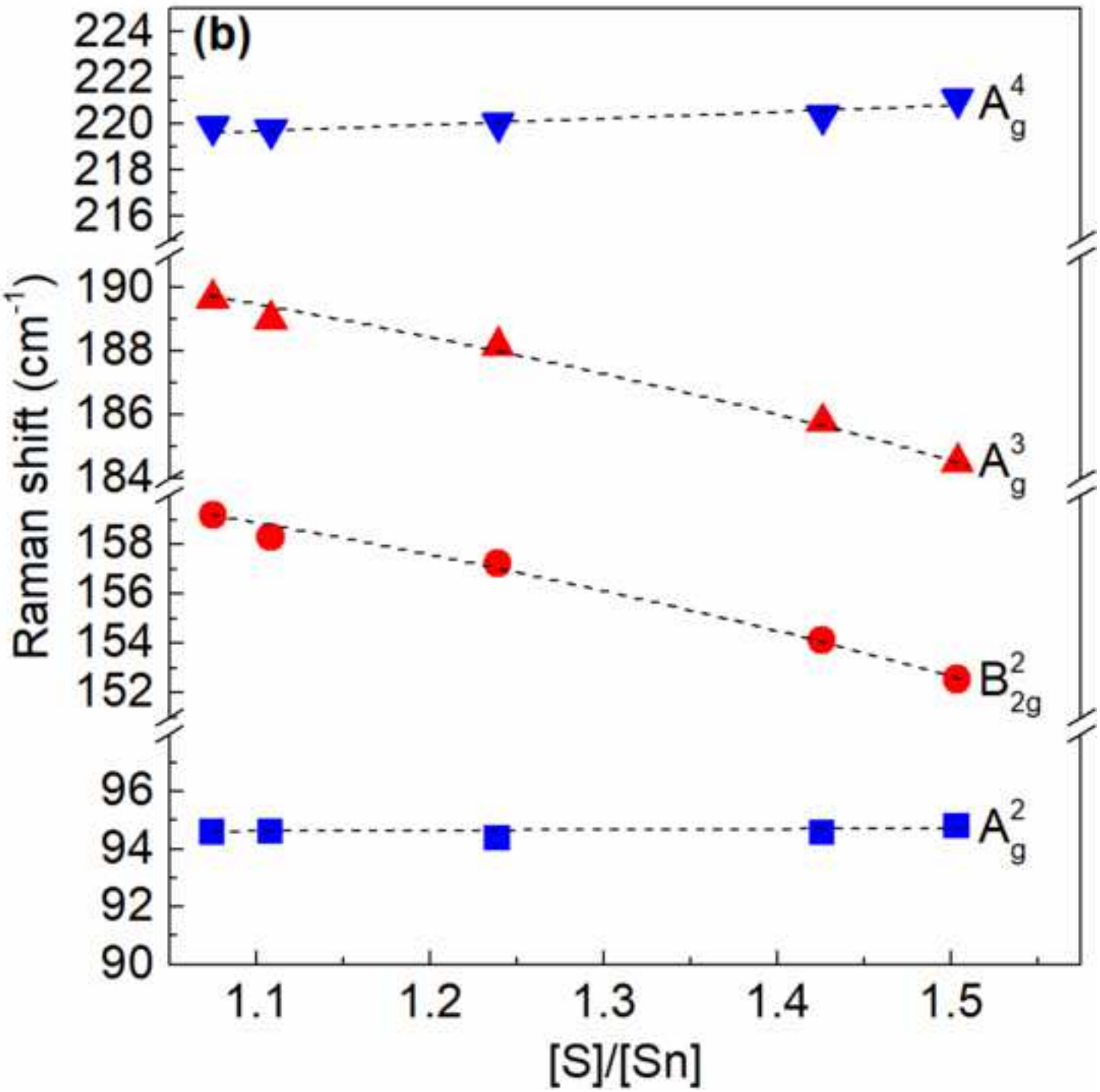

Figure 7

Click here to download high resolution image

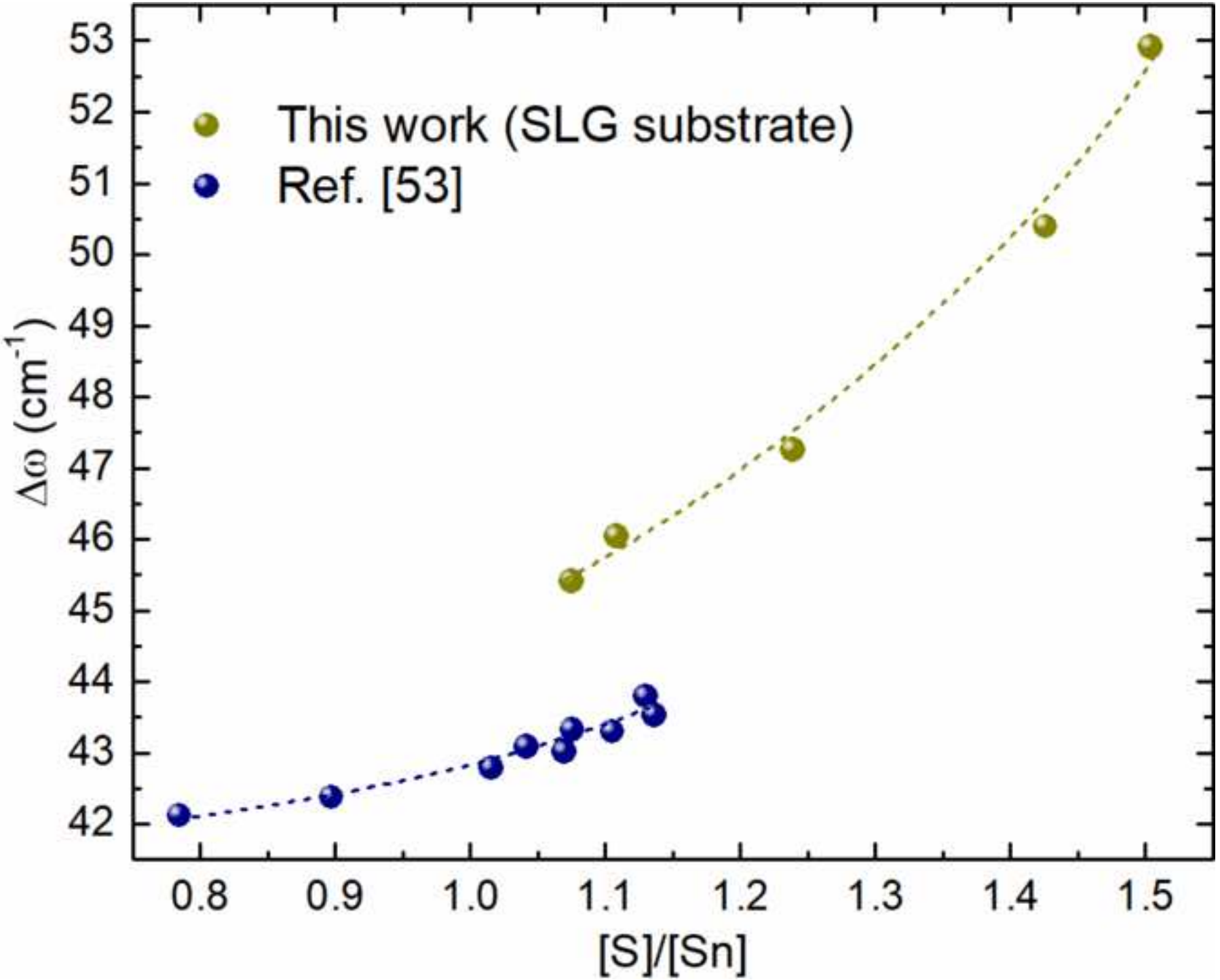

Figure 8

Click here to download high resolution image

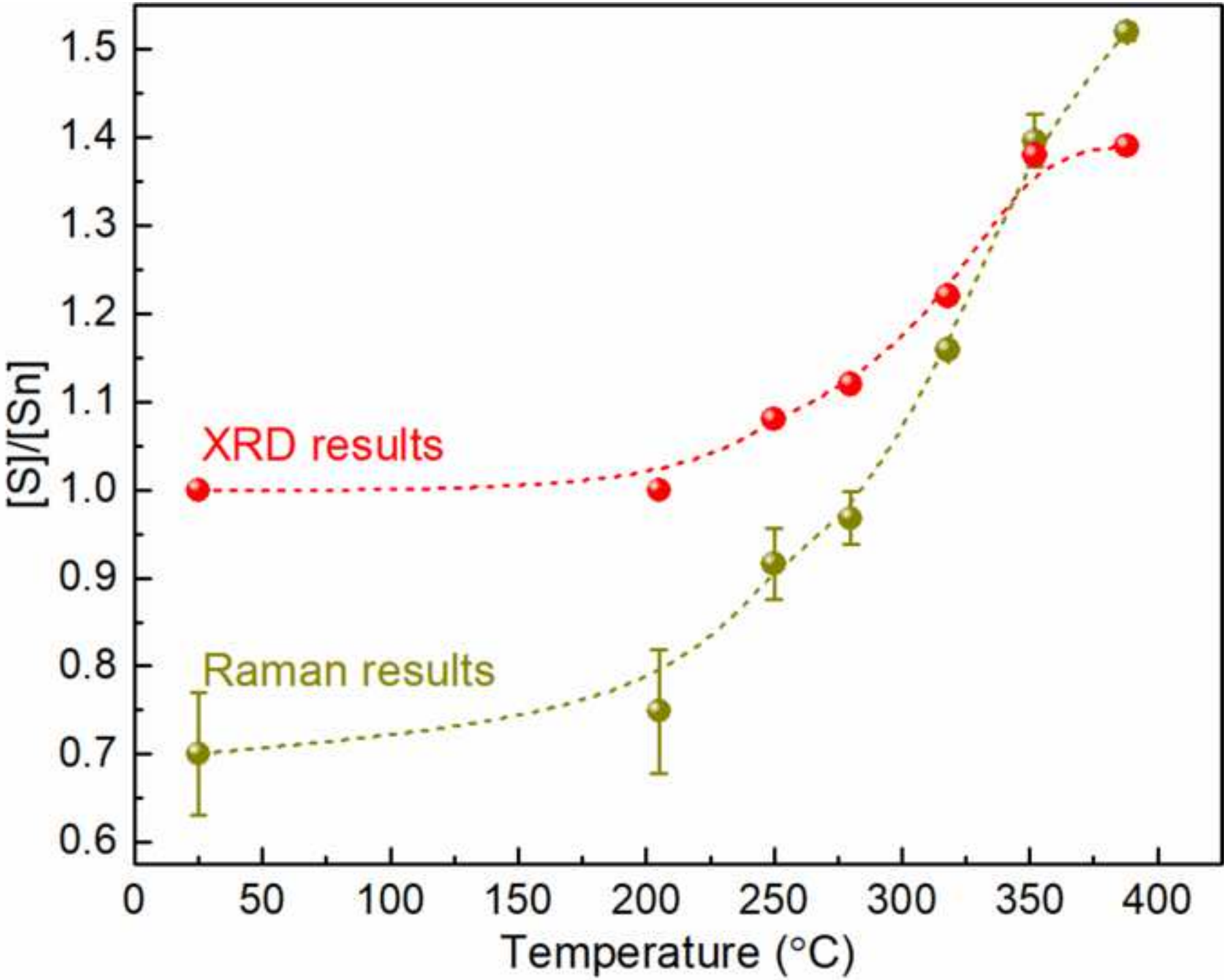

Table(s)

Table 1. *Agreement factors, cell parameters, cell volume, volume per formula unit (V/Z) and averaged microstructure parameters obtained from the Rietveld refinements on pure α-SnS and π-SnS thin film samples.*

Phase	Structure, space group, Z	R_{wp}	R_B	*a* (Å)	*b* (Å)	*c* (Å)	V ($Å^3$)	V/Z ($Å^3$)	Apparent crystal size (nm)	Microstrain $(\delta d/d)\cdot 10^4$
α-SnS	Orthorhombic, *Pnma*, 4	6.87	3.69	11.2137	3.9917	4.3151	193.150	48.29	280	13
π-SnS	Cubic, $P3_12$, 32	5.47	2.95	11.62658	-	-	1571.65	49.11	>1000	1.2

Table 2. *Position of Raman peaks of α-SnS and π-SnS phases. Results from previous experimental and theoretically calculated wavenumbers are also presented, together with proposed symmetry assignment.*

α-SnS					**π-SnS**				
λ* (nm)	**Exp This work (cm^{-1})**	**Exp [49,48] (cm^{-1})**	**Calc. [34] (cm^{-1})**	**Sym. [34]**	**λ* (nm)**	**Exp This work (cm^{-1})**	**Exp [38] (cm^{-1})**	**Calc. [34] (cm^{-1})**	**Sym [34]**
	40.7	40, 47	41	A_g^1		39.4		36, 36, 39	E, T, A
						45.9		43, 47, 48	T, T, E
	50.1	49, 50	48	B_{2g}^2		49.9		49, 50, 51	A, T, T
						58.9	59	54, 56, 56, 58, 59, 61, 62, 64	T, E, T, T, E, T, A, T
All	68.3	70, 58	66, 67	B_{3g}^1, B_{1g}^1	785	70.8	71	66, 68, 69, 71, 71, 72	E, A, T, T, E, T
633	77.6	85, 78	80	B_{1g}^2					
					All	85.2		79, 79, 81, 84, 86	T, A, E, A, T
					All	90.3	90	88, 89, 92	T, T, T
785	96.4	95, 111	92	A_g^2	785	96.8		98, 99, 103	T, T, T
					All	111.0	112	107, 107, 112	T, E, A
					442	121.9	123	116, 118	T, A
442	163.3	164, 160	161	B_{2g}^3					
					442	173.4	176	165, 166, 166, 168, 173, 174, 177, 178, 180, 183	A, E, T, T, A, T, E, T, T,E
532/633	191.8	192, 194	189	A_g^3	325	192.1	192	187, 195, 197	A, T, T
	–	208, –	203	B_{3g}^2	325/785	204.1	202	201, 202, 202, 207, 209, 210, 212, 214	T, T, A, T, T, E, T, E
785	219.5	218, 216	218, 220	B_{1g}^1, A_g^4	785	220.8	224	219, 220, 220, 221, 222, 224	A, E, T, A, T, T
					442	230.3		227, 229, 229, 239	T, E, T, T
785	263.3	–, 264	275	B_{1g}^2	442/432/633	262.9		242, 249, 252, 257, 257, 257, 263, 266	T, T, T, A, E, T, A, T
					325/633	276.5		269	T
633/785	286.5	290, –		A_g^2+A_g^3**					

**Optimal excitation wavelength for the assessment of the each peak. The 514.5 is discarded for its preferential polarization signal dependence due to the configuration of the system.*

***Multimode assignment proposed in this work, in contrast to the data from Ref. [49].*

Supplementary Material

Click here to download Supplementary Material: Supporting information_rev_fin.pdf

*Graphical Abstract

$$[S]/[Sn] = (0.6 \times \Delta\omega) - (0.005 \times \Delta\omega^2) - 15$$

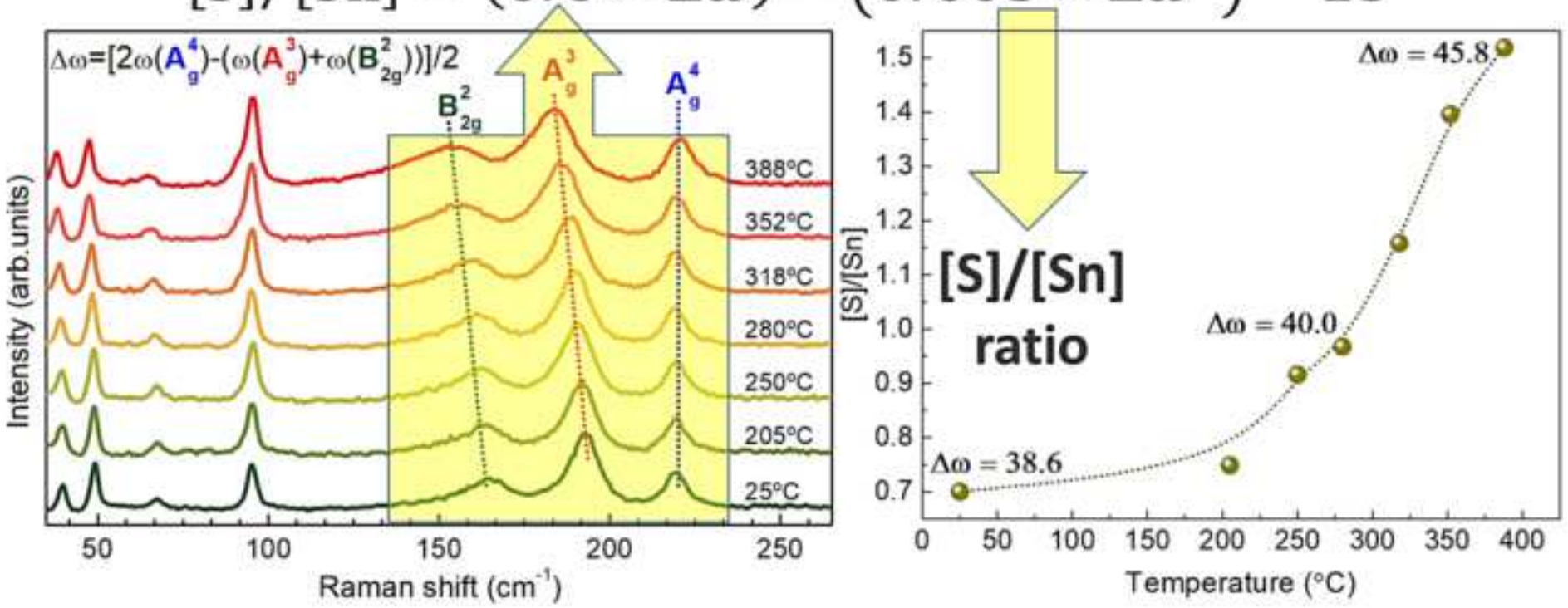

***Declaration of Interest Statement**

Declaration of interests

☒ The authors declare that they have no known competing financial interests or personal relationships that could have appeared to influence the work reported in this paper.

☐The authors declare the following financial interests/personal relationships which may be considered as potential competing interests: